Molecular Cell

Article

Lysosomal cystine governs ferroptosis sensitivity in cancer via cysteine stress response

Graphical abstract

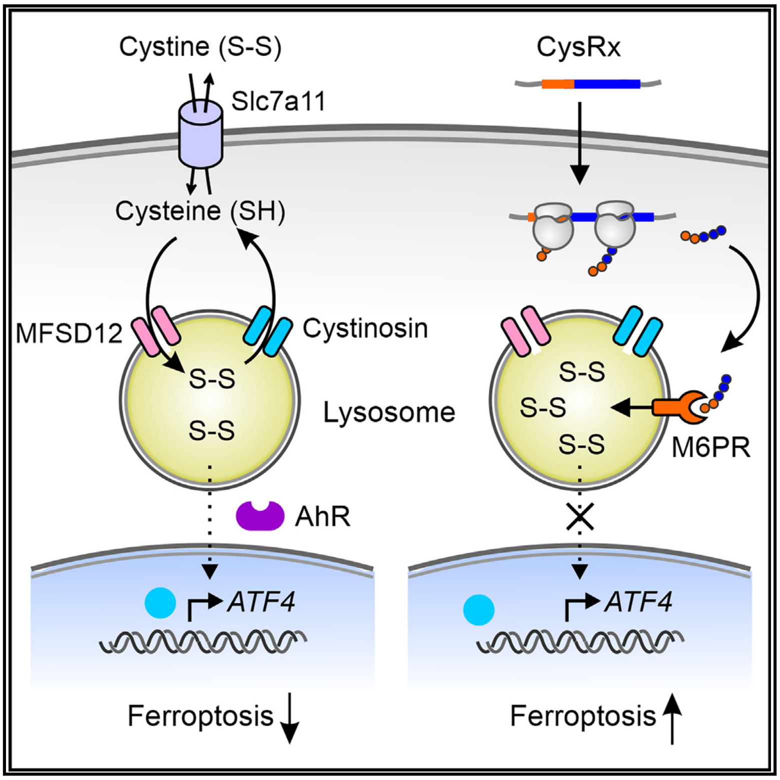

Highlights

- Cysteine depletion triggers adaptive ATF4 expression at the transcriptional level
- Lysosomal cystine shortage induces ATF4 expression via the AhR signaling pathway
- Attenuated cysteine stress response sensitizes ferroptosis upon cysteine starvation
- CysRx elicits cancer cell ferroptosis via intracellular nutrient reprogramming

Authors

Robert V. Swanda, Quanquan Ji, Xincheng Wu, ..., Saori Uematsu, Yizhou Dong, Shu-Bing Qian

Correspondence

sq38@cornell.edu

In brief

Swanda et al. reported that lysosomal cystine regulates the adaptative ATF4 expression, whereas cytosolic cysteine determines the ferroptosis sensitivity. By controlling the intracellular balance between cysteine and cystine, the synthetic CysRx reagent exhibits therapeutic potential by attenuating cysteine stress response and maximizing cancer cell ferroptosis.

Swanda et al., 2023, Molecular Cell *83*, 3347–3359
September 21, 2023 © 2023 Elsevier Inc.
https://doi.org/10.1016/j.molcel.2023.08.004

CellPress

Molecular Cell

CellPress

Article

Lysosomal cystine governs ferroptosis sensitivity in cancer via cysteine stress response

Robert V. Swanda,[1] Quanquan Ji,[2] Xincheng Wu,[2] Jingyue Yan,[3] Leiming Dong,[2] Yuanhui Mao,[2] Saori Uematsu,[2] Yizhou Dong,[3] and Shu-Bing Qian[1,2,4,*]
[1]Graduate field of Biomedical and Biological Sciences, Cornell University, Ithaca, NY 14853, USA
[2]Division of Nutritional Sciences, Cornell University, Ithaca, NY 14853, USA
[3]Division of Pharmaceutics and Pharmacology, College of Pharmacy, The Ohio State University, Columbus, OH 43210, USA
[4]Lead contact
*Correspondence: sq38@cornell.edu
https://doi.org/10.1016/j.molcel.2023.08.004

SUMMARY

The amino acid cysteine and its oxidized dimeric form cystine are commonly believed to be synonymous in metabolic functions. Cyst(e)ine depletion not only induces amino acid response but also triggers ferroptosis, a non-apoptotic cell death. Here, we report that unlike general amino acid starvation, cyst(e)ine deprivation triggers ATF4 induction at the transcriptional level. Unexpectedly, it is the shortage of lysosomal cystine, but not the cytosolic cysteine, that elicits the adaptative ATF4 response. The lysosome-nucleus signaling pathway involves the aryl hydrocarbon receptor (AhR) that senses lysosomal cystine via the kynurenine pathway. A blockade of lysosomal cystine efflux attenuates ATF4 induction and sensitizes ferroptosis. To potentiate ferroptosis in cancer, we develop a synthetic mRNA reagent, CysRx, that converts cytosolic cysteine to lysosomal cystine. CysRx maximizes cancer cell ferroptosis and effectively suppresses tumor growth *in vivo*. Thus, intracellular nutrient reprogramming has the potential to induce selective ferroptosis in cancer without systematic starvation.

INTRODUCTION

Cells maintain intracellular amino acid homeostasis via cytosolic translational reprogramming and nuclear transcriptional adaptation. Upon amino acid restriction, the integrated stress response (ISR) is typically induced via general control nonderepressible 2 (GCN2) kinase.[1,2] Activated GCN2 phosphorylates eukaryotic initiation factor 2α (eIF2α), resulting in translational reprogramming that inhibits general protein synthesis but paradoxically increases the translation of a subset of messenger RNAs (mRNAs).[3,4] In mammalian cells, the most notable example of selective translation during ISR is activating transcription factor 4 (ATF4), a bZip transcription factor that promotes the expression of genes involved in antioxidant response and amino acid biosynthesis and transport.[5] Notably, ATF4 acts as a survival factor for many cancer cells, and high ATF4 expression is often associated with poor prognosis.[6] It is widely believed that the primary regulation of ATF4 expression is through translational control of preexisting mRNA.[7,8] The transcriptional regulation of ATF4, however, remains surprisingly obscure.

Our current understanding of amino acid response has been largely driven by studies based on full amino acid starvation. It remains unclear whether single amino acid deprivation triggers the common ISR or elicits a unique cellular response. Cysteine, a semi-essential amino acid, is required for the synthesis of proteins and many intracellular metabolites such as glutathione (GSH), a primary cellular antioxidant.[9] Cysteine mainly exists as cystine in the extracellular space and is actively transported into cells via the cystine-glutamate antiporter system X_c^-.[10] Once inside cells, each cystine is reduced to two molecules of cysteine. Despite its vital roles in protein synthesis and redox homeostasis, cysteine is surprisingly maintained at low levels in the cytosol.[11] A large fraction of cysteine is imported into the lysosome by MFSD12 (major facilitator superfamily domain containing 12),[12] whose function is coupled with the lysosomal V-ATPase pump.[13] Lysosomal cystine can be mobilized to supply intracellular cysteine by the transporter cystinosin (CTNS), whose loss-of-function mutations cause the lysosomal storage disorder cystinosis.[14] Cysteine and cystine are commonly believed to be synonymous in metabolic functions, but little is known about how the physiological cycling between cysteine and cystine contributes to general amino acid response.

Cysteine depletion leads to ferroptosis, a peroxidation-driven and iron-catalyzed form of non-apoptotic cell death.[15,16] Recent studies revealed key regulatory pathways of ferroptosis in cytosol and mitochondria, as exemplified by GSH peroxidase 4 (GPX4),[17] ferroptosis suppressor protein 1 (FSP1),[18,19] and dihydroorotate dehydrogenase (DHODH).[20] Although lysosomes have emerged as signaling hubs for amino acid metabolism,[21] the role of lysosomal cystine in ferroptosis remains a fundamental knowledge gap. Inducible ferroptosis has been harnessed for cancer therapy

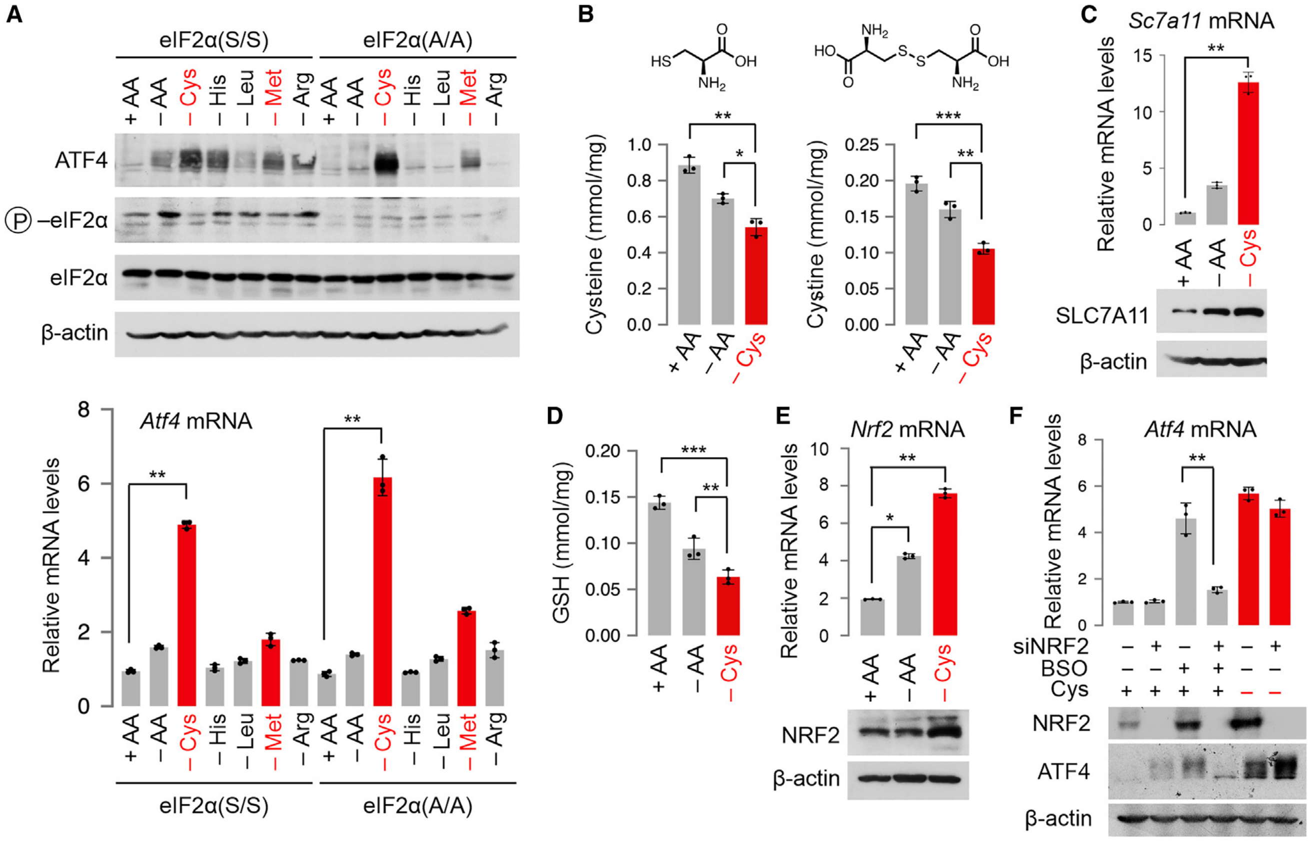

Figure 1. Cysteine deprivation induces ATF4 expression independent of the eIF2α signaling pathway

(A) The top panel shows the western blotting of eIF2α (S/S) and eIF2α (A/A) MEF cells after 8 h of amino acid starvation. The bottom panel shows RT-qPCR results of *Atf4* (normalized to *Gapdh*) in eIF2α (S/S) and eIF2α (A/A) MEF cells after 8 h of amino acid starvations. Error bars, mean ± SEM; two-tailed t test, $^{**}p < 0.01$, $n = 3$ biological replicates.

(B) Total cysteine (left) and cystine (right) levels in MEF cells after 12 h of amino acid starvation. Both measurements are normalized to protein levels. Error bars, mean ± SEM; two-tailed t test, $^{*}p < 0.05$, $^{**}p < 0.01$, $^{***}p < 0.001$, $n = 3$ biological replicates.

(C) The top bar graph shows the RT-qPCR results of *Slc7a11* (normalized to *Gapdh*) in MEF cells after 8 h of amino acid starvation. Error bars, mean ± SEM; two-tailed t test, $^{**}p < 0.01$, $n = 3$ biological replicates. The bottom panel shows the representative western blotting of SLC7A11 in starved MEF cells.

(D) Total GSH levels in MEF cells after 12 h of amino acid starvations are normalized to protein levels. Error bars, mean ± SEM; two-tailed t test, $^{**}p < 0.01$, $^{***}p < 0.001$, $n = 3$ biological replicates.

(E) The top bar graph shows the RT-qPCR results of *Nrf2* (normalized to *Gapdh*) in MEF cells after 8 h of amino acid starvation. Error bars, mean ± SEM; two-tailed t test, $^{*}p < 0.05$, $^{**}p < 0.01$, $n = 3$ biological replicates. The bottom panel shows the representative western blotting of NRF2 in starved MEF cells.

(F) MEF cells with or without Nrf2 knockdown were subject to either 8 h of BSO (10 μM) treatment or 8 h of cysteine starvation. The top bar graph shows the RT-qPCR results of *Atf4* (normalized to *Gapdh*). Error bars, mean ± SEM; two-tailed t test, $^{**}p < 0.01$, $n = 3$ biological replicates. The bottom panel shows the representative western blotting of ATF4 in starved MEF cells.

with many ferroptosis modulators tested for therapeutic potential. However, the adaptative ATF4 response inevitably counteracts the effectiveness of ferroptosis in cancer. It is thus highly desirable if therapeutic cysteine intervention can be de-coupled from adaptative ATF4 induction. A better understanding of cysteine stress response will facilitate the rational design of selective ferroptosis in cancer.

RESULTS

Cysteine stress response is independent of ISR

To compare full amino acid starvation with single amino acid deprivation, we took advantage of a mouse embryonic fibroblast (MEF) cell line harboring a non-phosphorylatable eIF2α in which the serine 51 (S/S) was mutated to an alanine (A/A).[22] Wild-type eIF2α (S/S) cells readily responded to whole amino acid starvation by showing increased eIF2α phosphorylation and robust ATF4 induction (Figure 1A), which were abolished in eIF2α (A/A) cells. Single amino acid withdrawal, however, resulted in varied ATF4 levels. Notably, cysteine starvation triggered the strongest ATF4 expression despite the minimal effect on eIF2α phosphorylation. Strikingly, a potent ATF4 induction was maintained in eIF2α (A/A) cells upon withdrawal of cysteine but not histidine, leucine, or arginine from the medium (Figure 1A). The eIF2α-independent ATF4 induction was also seen after removal of methionine, a cysteine precursor, albeit to a lower extent. The similar finding holds true in MEF cells lacking GCN2 (Figure S1A). Further confirming the eIF2α independency, the cysteine shortage-induced ATF4 upregulation was insensitive to ISRIB, a small-molecule ISR inhibitor (Figure S1B). Using a firefly luciferase (Fluc) reporter bearing the 5′ untranslated region (UTR) of *ATF4*, we found comparable Fluc levels between whole amino acid starvation and cysteine deprivation (Figure S1C), suggesting that mechanisms beyond translational control likely contribute to the ATF4 induction upon cysteine shortage. We next measured *Atf4* mRNA levels in starved cells using RT-qPCR. In comparison to full amino acid starvation that induced *Atf4* expression by ~2-fold, cysteine deprivation increased *Atf4* mRNA levels by >5-fold (Figure 1A, bottom panel). The differential induction of Atf4 between full amino acid starvation and cysteine deprivation was further confirmed by RNA sequencing (RNA-seq) (Figure S1D). The transcriptional upregulation of ATF4 was also seen in HEK293 cells (Figure S1E) and confirmed by a Fluc reporter driven by the *ATF4* promoter (Figure S1F). Besides MEFs and HEK293 cells, we observed the similar cysteine stress response in several human and mouse cancer cell lines (Figure S1G). Therefore, cysteine shortage induces a unique transcriptional induction of ATF4 in the nucleus, which surprisingly overcomes the translational control of ATF4 mediated by eIF2α phosphorylation.

Intracellular cysteine can be stored in lysosomes in the form of cystine. We used high-performance liquid chromatography to quantify intracellular cysteine and cystine levels. As expected, cysteine deprivation from the medium lowered intracellular levels of both cystine and cysteine (Figure 1B). Similar to cysteine starvation, treatment with erastin, a potent system X_c^- inhibitor,[15] also decreased intracellular cysteine and cystine levels (Figure S1H). Likewise, erastin treatment led to a robust ATF4 induction independent of eIF2α phosphorylation (Figure S1I). Notably, cysteine withdrawal led to a marked increase of SLC7A11, an essential subunit of the system X_c^- antiporter (Figure 1C). Additionally, cysteine depletion upregulated the expression of cystathionine γ-lyase (CSE) (Figure S1J), an enzyme that breaks down cystathionine into cysteine. Both SLC7A11 and CSE are downstream targets of ATF4,[23] representing an adaptive cellular response to mitigate cysteine shortage.

It is intriguing to find that full amino acid starvation is less potent in ATF4 induction despite the fact that the medium also lacks cysteine. We found that withdrawal of cysteine alone resulted in a more significant decrease of intracellular cysteine and cystine levels than full amino acid starvation (Figure 1B). This is likely due to their differential effects on global protein synthesis. Indeed, puromycin labeling revealed a rapid inhibition of global protein synthesis upon full amino acid starvation but not upon cysteine depletion (Figure S2A). This is in line with the notion that cysteine starvation minimally induces ISR. Additionally, cysteine does not seem to affect mTOR signaling pathway,[24] although this feature could be cell-type specific.[17] Unlike full amino acid starvation, cysteine deprivation had little effect on autophagy (Figure S2B). The continuous *de novo* protein synthesis under cysteine restriction is expected to further deplete the intracellular cysteine pool. Supporting this notion, translation inhibition by cycloheximide (CHX) partially restored the cysteine and cystine levels (Figure S2C), indicating that translation is a major consumer of intracellular cysteine.

Cysteine stress response is independent of NRF2

In addition to protein synthesis, cysteine is the rate-limiting precursor for the synthesis of intracellular metabolites such as GSH.[9] Indeed, there was a 50% reduction of GSH in cysteine-starved cells (Figure 1D). As expected, a decline in intracellular GSH led to oxidative stress response as evidenced by the elevated NRF2 (nuclear factor erythroid 2–related factor 2) [25] (Figure 1E). Given the much higher NRF2 induction under cysteine starvation, we wondered whether the robust ATF4 upregulation was simply a result of excessive oxidative stress response.[26] However, the antioxidant ascorbic acid had little effect on ATF4 induction upon cysteine starvation (Figure S2D). By contrast, the same treatment attenuated ATF4 expression induced by homocysteic acid (HCA), a potent oxidative stress inducer.[26] To substantiate this finding further, we genetically silenced NRF2 in MEF cells and induced oxidative stress response by buthionine sulfoximine (BSO), which inhibits GSH biosynthesis. Knocking down NRF2 suppressed ATF4 expression induced by BSO but had little effect on cysteine-starved cells (Figure 1F). Therefore, other mechanisms are likely in place to mediate the cysteine stress response.

Cysteine stress response is sensitive to lysosomal cystine

A recent study reported that intracellular cysteine is imported into the lysosome by MFSD12[12] in a process coupled with the V-ATPase pump[13] (Figure 2A). Once inside the lysosome, cysteine is oxidized to cystine (Figure S2E). Indeed, V-ATPase inhibition by bafilomycin A1 (BafA1) resulted in an increase of cysteine and a corresponding decrease in cystine (Figure 2B). Remarkably, the presence of BafA1 greatly potentiated ATF4 induction in cysteine-starved cells (Figure 2C). Since the cytosolic cysteine level was partially restored in the presence of BafA1, this result suggests that it is the shortage of lysosomal cystine that triggers *Atf4* expression. The same result was obtained by applying another V-ATPase inhibitor concanamycin A (ConA) (Figures S2F and S2G). The transcriptional upregulation of ATF4 upon V-ATPase inhibition was further confirmed by the *Atf4* promoter-driven reporter assay (Figure 2D). We next examined NRF2 activity using a Fluc reporter containing the antioxidant-responsive element (ARE). V-ATPase inhibition evidently prevented NRF2 activation (Figure S2H), which is in line with the elevated cysteine levels in the cytosol. We conclude that the transcriptional regulation of ATF4 is governed by lysosomal cystine in an ISR- and NRF2-independent manner.

The lysosomal cystine undergoes efflux via CTNS,[14] forming a cystine-to-cysteine cycle. As expected, silencing *CTNS* led to an increase of cystine and a decrease of cysteine levels (Figures 2E and S3A). Remarkably, ATF4 induction upon cysteine withdrawal was largely blunted in the absence of CTNS (Figure 2F), and this was further confirmed by the *Atf4* promoter-driven reporter assay (Figure S3B). The attenuated ATF4 expression was rescued by reintroducing exogenous CTNS (Figures S3C and S3D), excluding the possibility of off targeting by short hairpin RNAs (shRNAs). Therefore, an accumulation of lysosomal cystine appears to attenuate ATF4 expression. Notably, cells lacking CTNS exhibited increased NRF2 activation (Figure S3E), which is in line with the lowered cysteine levels. In comparison to control cells, CTNS

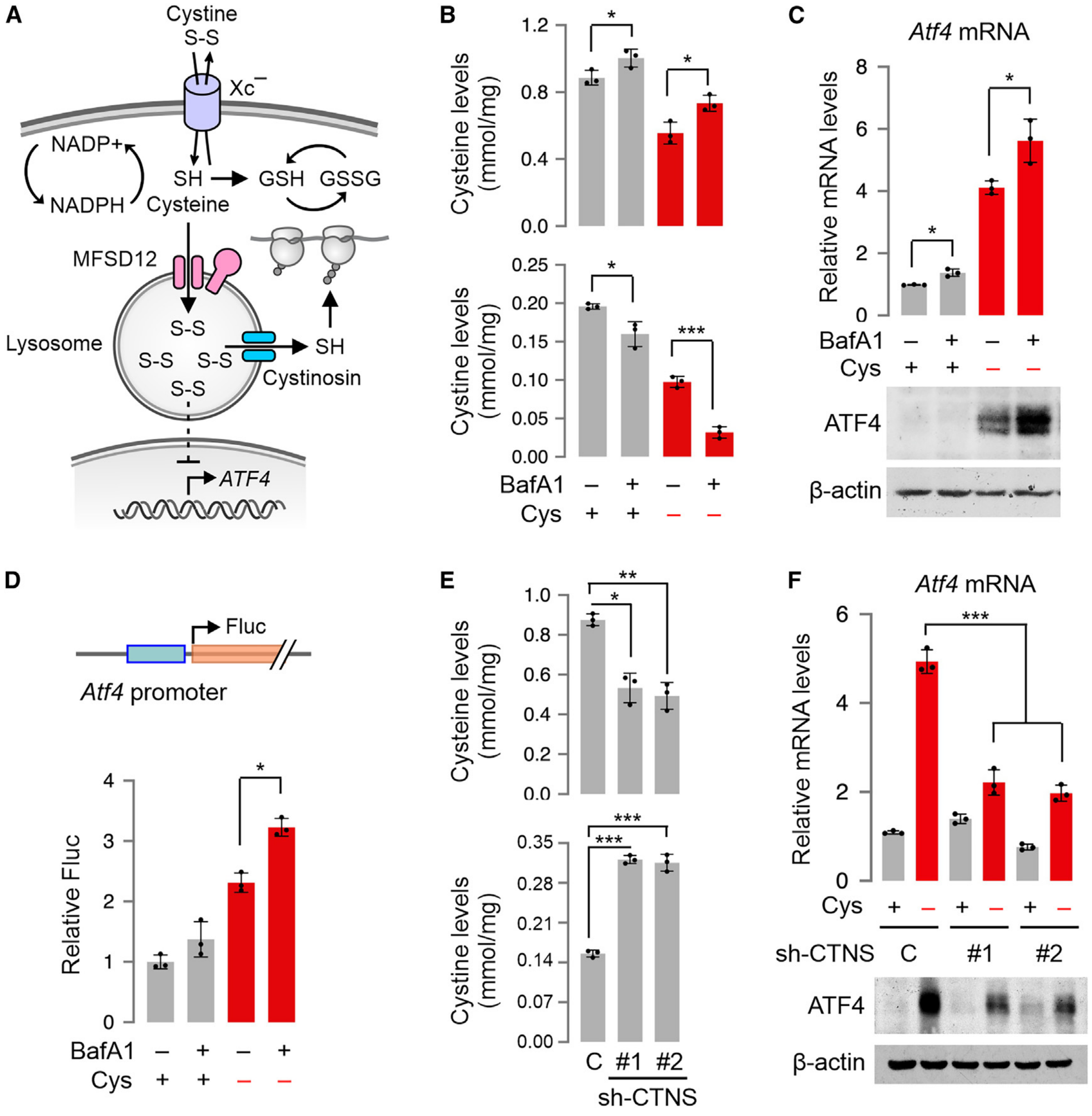

Figure 2. Lysosomal cystine controls transcriptional regulation of ATF4

(A) Schematic of intracellular cysteine and cystine metabolism, storage, and function.

(B) Total cysteine (top) and cystine (bottom) levels in MEF cells treated with bafilomycin A (50 nM for 12 h) with or without cysteine deprivation. Both measurements are normalized to protein levels. Error bars, mean ± SEM; two-tailed t test, $^*p < 0.05$, $^{***}p < 0.001$, n = 3 biological replicates.

(C) The top bar graph shows the RT-qPCR results of *Atf4* (normalized to *Gapdh*) in MEF cells treated with bafilomycin A (50 nM for 8 h) with or without cysteine deprivation. Error bars, mean ± SEM; two-tailed t test, $^*p < 0.05$, n = 3 biological replicates. The bottom panel shows the representative western blotting of ATF4 in MEF cells.

(D) The top panel shows the illustration of a Fluc reporter driven by the *Atf4* promoter. The bar graph shows the relative Fluc activities normalized to Renilla luciferase in transfected MEF cells treated with bafilomycin A (50 nM for 8 h) with or without cysteine deprivation. Error bars, mean ± SEM; two-tailed t test, $^*p < 0.05$, n = 3 biological replicates.

(E) Total cysteine (top) and cystine (bottom) levels in MEF cells with or without CTNS knockdown. Both measurements are normalized to protein levels. Error bars, mean ± SEM; two-tailed t test, $^*p < 0.05$, $^{**}p < 0.01$, $^{***}p < 0.001$, n = 3 biological replicates.

(F) The top bar graph shows the RT-qPCR results of *Atf4* (normalized to *Gapdh*) in MEF cells with or without CTNS knockdown before and after cysteine deprivation. Error bars, mean ± SEM; two-tailed t test, $^{***}p < 0.001$, n = 3 biological replicates. The bottom panel shows the representative western blotting of ATF4 in MEF cells.

silencing readily suppressed global protein synthesis in cysteine-starved cells (Figures S3F and S3G), a strong indication of depleted cytosolic cysteine. Therefore, even under the shortage of cysteine, an accumulation of lysosomal cystine attenuates the ATF4 response.

To further confirm that the attenuated ATF4 response in cells lacking CTNS is attributed to the accumulated lysosomal cystine, we treated cells with cysteamine, which resolves lysosomal cystine accumulation independent of CTNS[27] (Figure S3H). As expected, cysteamine treatment readily

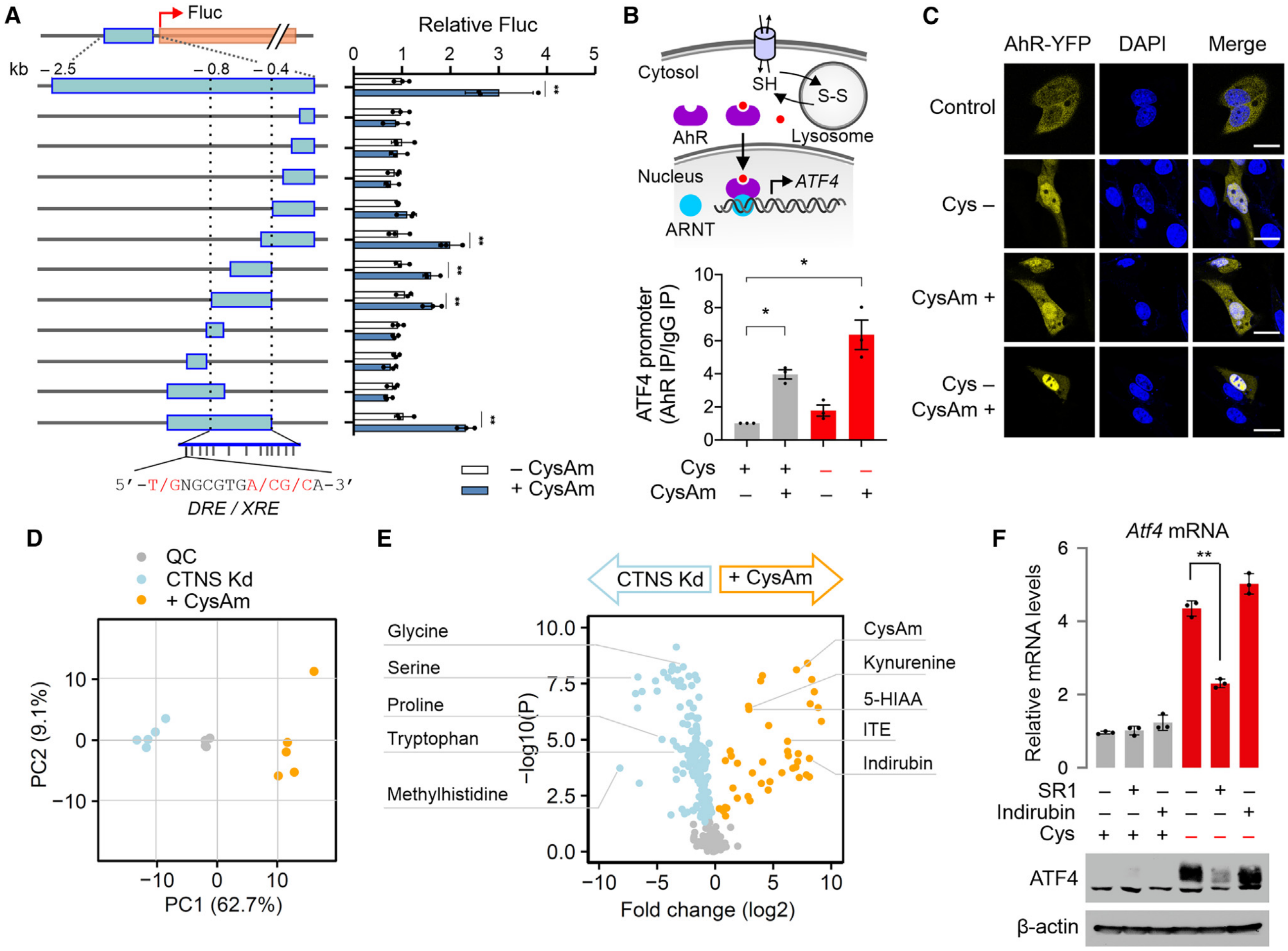

Figure 3. Lysosomal cystine mediates cysteine stress response via the AhR signaling pathway

(A) The left panel shows the illustration of the *Atf4* promoter region with various truncation. The bottom panel highlights the *DRE/XRE* consensus sequences. MEF cells transfected with Fluc reporters driven by truncated Atf4 promoter regions were subjected to cysteamine (0.5 mM) treatment (blue bars) or vehicle control (white bar) for 8 h followed by luminometry. Fluc activities are normalized to Renilla luciferase. Error bars, mean ± SEM; two-tailed t test, $^{**}p < 0.01$, n = 3 biological replicates.

(B) The top panel shows the simplified AhR signaling pathway. Upon binding of ligands (red dots), AhR translocates into the nucleus and dimerizes with ARNT. The bottom panel shows the ChIP analysis in MEF cells after 12 h of cysteine starvation in the presence or absence of cysteamine (50 μM). ChIP was performed using AhR antibody followed by RT-qPCR of the *Atf4* promoter. Error bars, mean ± SEM; two-tailed t test, $^{*}p < 0.05$, n = 3 biological replicates.

(C) MEF cells transfected with AhR-YFP were subjected to 12 h of cysteine starvation in the presence or absence of cysteamine (50 μM). Nuclei were stained with DAPI. Scale bars, 20 μm.

(D) Principal component analysis based on the untargeted metabolomics data shows a clear separation between cysteamine treatment and CTNS knockdown.

(E) The volcano plot derived from the untargeted metabolomics highlights the top metabolites that increased (orange) or decreased (blue) in response to lysosomal cystine depletion after cysteamine treatment.

(F) The top bar graph shows the RT-qPCR results of *Atf4* (normalized to *Gapdh*) in MEF cells treated with SR1 (200 nM) or indirubin (2 μM) before and after cysteine deprivation. Error bars, mean ± SEM; two-tailed t test, $^{**}p < 0.01$, n = 3 biological replicates. The bottom panel shows the representative western blotting of ATF4 in MEF cells treated with AhR modulators.

decreased lysosomal cystine with a corresponding increase of cysteine in the cytosol (Figure S3I). Importantly, cysteamine treatment led to a pronounced ATF4 induction even under the nutrient-rich condition (Figure S3J). Therefore, without absolute starvation, a decrease in lysosomal cystine is sufficient to trigger ATF4 induction. This was further supported by the *Atf4* promoter-driven reporter assay (Figure S3K). Altogether, we demonstrate the existence of a signaling pathway linking lysosomal cystine and nuclear *Atf4* gene expression.

Cysteine stress response involves the AhR signaling pathway

To probe how a shortage of lysosomal cystine leads to transcriptional response of ATF4, we dissected the *Atf4* promoter region using the Fluc reporter assay. Like the endogenous *Atf4*, a reporter containing the 2.5-kb region upstream of the *Atf4* transcription start site showed a robust response to cysteamine treatment that leads to lysosomal cystine depletion (Figure 3A). Targeted deletion of this upstream region revealed a sub-region between −400 and −800 bp that was critical for maintaining the cysteamine sensitivity. Analysis of this critical sub-region identified 13 motifs with similarity to dioxin response element (DRE), which is also referred to as xenobiotic response element (XRE) (Figure 3A, bottom panel). The DRE/XRE is recognized by activated aryl hydrocarbon receptor (AhR),[28] which senses a wide range of environmental stimuli as well as intracellular metabolites.[29] To confirm the participation of AhR in the transcriptional regulation of ATF4, we conducted chromatin immunoprecipitation (ChIP) assays using AhR-specific antibodies. Lysosomal cystine depletion by cysteamine treatment increased the binding of AhR to the *Atf4* promoter (>3-fold, Figure 3B), which was more prominent under cysteine starvation. The similar result was obtained in cells treated with BafA1 (Figure S3L). Furthermore, knocking down AhR using shRNA prevented ATF4 induction in cysteine-starved cells (Figure S3M), confirming AhR-mediated cysteine response.

AhR normally resides in the cytoplasm as an inactive complex. Upon ligand binding, AhR translocates into the nucleus, where it dimerizes with ARNT (aryl hydrocarbon receptor nuclear translocator) and subsequently binds genomic regions containing DRE/XRE.[30] To monitor AhR localization in response to lysosomal cystine shortage, we transfected cells with AhR-YFP that were primarily localized in the cytoplasm under the normal growth condition. Cysteine withdrawal resulted in a nuclear accumulation of AhR-YFP (Figure 3C), an indication of AhR activation. Cysteamine treatment also led to nuclear translocation of AhR-YFP even under the nutrient-rich condition. Therefore, a cystine shortage in lysosomes is sufficient to activate AhR. Adding cysteamine to cysteine-starved cells substantiated the nuclear localization of AhR-YFP (Figure 3C). Likewise, BafA1 treatment readily triggered nuclear re-localization of AhR-YFP, especially under cysteine starvation (Figure S3N). Collectively, these results indicate that AhR acts as a lysosome-nucleus signaling pathway by responding to lysosomal cystine shortage.

AhR senses lysosomal cystine levels via the kynurenine pathway

To identify potential AhR ligands in response to cystine shortage in lysosomes, we conducted untargeted metabolomics on MEF cells with either lysosomal cystine accumulation (i.e., CTNS knockdown) or depletion (i.e., cysteamine treatment). To minimize alterations of amino acid metabolism, cells were grown in complete media. From five replicates of each condition, the principal component analysis (PCA) of metabolite profiling revealed a clear separation between cysteamine treatment and CTNS knockdown (Figure 3D; Table S1). Hierarchical clustering analysis revealed significant association between lysosome cystine and amino acid metabolism (Figures S4A and S4B). Volcano plot analysis highlighted the top metabolites that increased or decreased in response to lysosomal cystine depletion (Figure 3E). Although cysteamine was recovered as the top metabolite as expected, many amino acids showed decreased levels upon cysteamine treatment (Figure 3E). Intriguingly, kynurenine metabolism was the top pathway affected by lysosomal cystine levels. Upon lysosomal cystine depletion, we observed an increase in kynurenine, kynurenic acid, and nicotinamide levels and a corresponding decrease of tryptophan and picolinic acid (Figure S4C). The kynurenine pathway is associated with the tryptophan catabolism and many kynurenine metabolites are endogenous ligands for AhR activation.[30] We also uncovered many indole derivatives known as endogenous AhR agonists such as 5-Hydroxyindole-3-acetic acid (5-HIAA), 2-(1′H-indole-3′-carbonyl)-thiazole-4-carboxylic acid methyl ester (ITE), and indirubin (Figures 3E and S4D). To substantiate this finding further, we treated cysteine-starved cells with AhR modulators. Although the AhR antagonist SR1 blocked ATF4 induction, the AhR activator indirubin further boosted the ATF4 levels (Figure 3F). The modest effect of indirubin suggests that activated AhR signaling is nearly maximal upon cysteine deprivation.

Cysteine stress response modulates ferroptosis sensitivity

Since cysteine is a potent regulator of ferroptosis,[11] the AhR-mediated cysteine response could modulate ferroptosis sensitivity. As expected, the cell death under cysteine restriction was prevented by ferrostatin-1 (a ferroptosis inhibitor) but not Z-VAD (an apoptosis inhibitor) or necrostatin (a necrosis inhibitor) (Figures S5A and S5B). By contrast, the reduced cell viability under full amino acid starvation was rescued by Z-VAD only. The apoptosis induced by full amino acid starvation was further evidenced by the cleaved caspase-3 (Figure S5C). One hallmark of ferroptosis is lipid peroxidation, which can be quantified by C11-BODIPY staining. Cysteine withdrawal, but not full amino acid starvation or leucine restriction, caused a large increase in lipid oxidation (Figure S5D). Additionally, silencing of *Slc7a11* promoted ferroptosis of cysteine-starved cells (Figures S5E and S5F). Since cysteine starvation minimally affects global translation, the continuous protein synthesis is expected to exacerbate cysteine depletion and subsequent ferroptosis. Supporting this notion, the increased ferroptosis susceptibility was prevented by CHX treatment (Figure S5G). Likewise, CHX also partially rescued ferroptosis induced by X_c^- inhibitors erastin and sulfasalazine (SSZ) (Figure S5H). These results confirm that the cysteine pool influences the ferroptosis susceptibility.

We next investigated the role of lysosomal cystine in ferroptosis. An inhibited lysosomal influx by BafA1 prevented ferroptosis in cysteine-starved cells and significantly reduced lipid oxidation (Figure 4A). Likewise, mobilizing cystine out of lysosomes via cysteamine treatment also rescued cells from ferroptosis and eliminated lipid oxidation (Figure 4B). Both treatments mitigate the cysteine scarcity in the cytosol at the expense of lysosomal cystine. We next examined whether a blockade of lysosomal cystine efflux would maximize ferroptosis. Indeed, cells lacking CTNS became extremely sensitive to cysteine withdrawal as evidenced by a drop in cell viability to ~10% (Figure 4C). This was due to ferroptosis because ferrostatin treatment largely rescued the cell viability (Figure S5I). Consistently, there was a surge in lipid oxidation in those cells (~60%) in comparison with wild-type cells (15%) (Figure 4C, right panel). The lack of CTNS also rendered cells highly susceptible to X_c^- inhibitors erastin and SSZ (Figure S5J). This was mainly due to the lysosomal cystine accumulation because cysteamine treatment rescued the ferroptotic cell death (Figure S5K).

An accumulation of cystine in lysosomes is accompanied with reduced levels of cytosolic cysteine, which likely explains the increased ferroptosis sensitivity. At the same time, the cystine

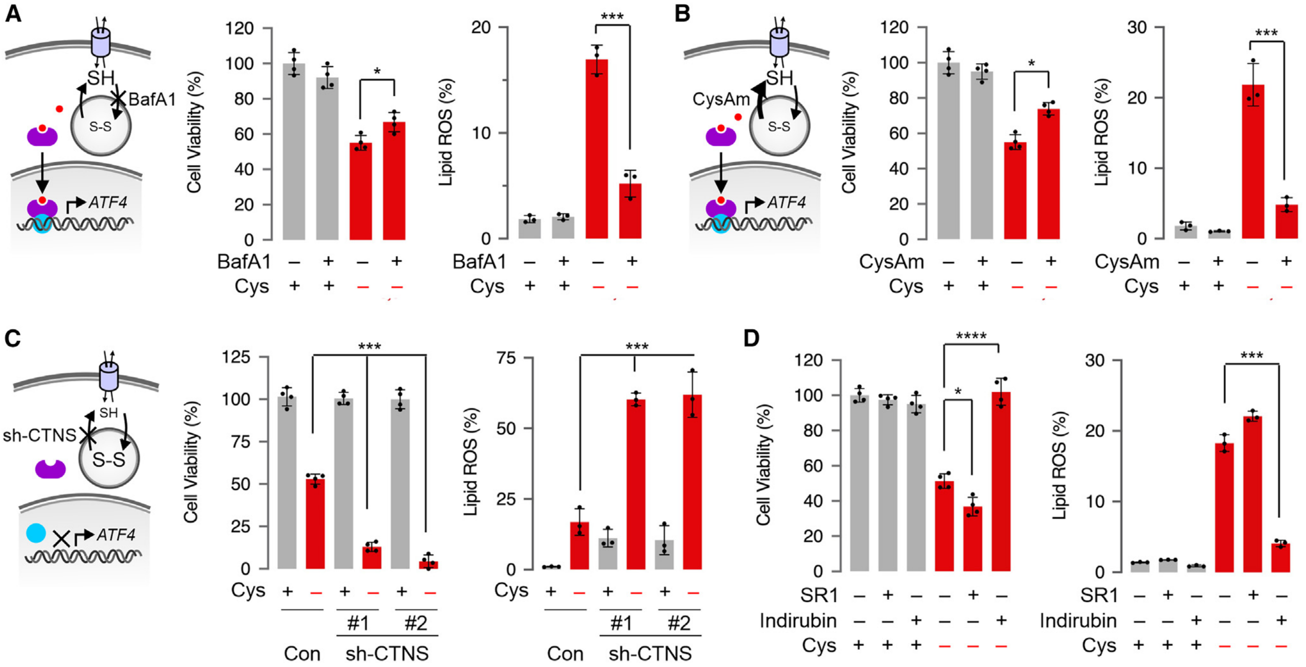

Figure 4. Lysosomal cystine modulates the cellular sensitivity to ferroptosis

(A) The left panel illustrates the cysteine (SH) and cystine (S-S) cycling with the action of BafA1. The middle panel shows the cell viability in MEF cells treated with BafA1 (50 nM) for 24 h with or without cysteine deprivation. Error bars, mean ± SEM; two-tailed t test, $^{*}p < 0.05$, n = 4 biological replicates. The right panel shows lipid ROS levels in MEF cells treated with BafA1 (50 nM for 18 h) with or without cysteine deprivation. The lipid ROS levels were quantified by C11-BODIPY staining and flow cytometry. Error bars, mean ± SEM; two-tailed t test, $^{***}p < 0.001$, n = 3 biological replicates.

(B) The left panel illustrates the cysteine (SH) and cystine (S-S) cycling with the action of cysteamine. The middle panel shows the cell viability in MEF cells treated with cysteamine (0.5 mM for 24 h) with or without cysteine deprivation. Error bars, mean ± SEM; two-tailed t test, $^{*}p < 0.05$, n = 4 biological replicates. The right panel shows lipid ROS levels in MEF cells treated with cysteamine (0.5 mM for 18 h) with or without cysteine deprivation. Error bars, mean ± SEM; two-tailed t test, $^{***}p < 0.001$, n = 3 biological replicates.

(C) The left panel illustrates the cysteine (SH) and cystine (S-S) cycling with the action of CTNS knockdown. The middle panel shows the cell viability in MEF cells with or without *CTNS* knockdown before and after 24 h cystine deprivation. Error bars, mean ± SEM; two-tailed t test, $^{***}p < 0.001$, n = 4 biological replicates. The right panel shows lipid ROS levels in MEF cells with or without CTNS knockdown before and after 18 h cysteine deprivation. Error bars, mean ± SEM; two-tailed t test, $^{***}p < 0.001$, n = 3 biological replicates. The middle panel shows the cell viability in MEF cells treated with SR1 (200 nM) or indirubin (2 μM) for 24 h with or without cysteine deprivation. Error bars, mean ± SEM; two-tailed t test, $^{*}p < 0.05$, $^{****}p < 0.0001$, n = 4 biological replicates.

(D) The right panel shows lipid ROS levels in MEF cells treated with SR1 (200 nM) or indirubin (2 μM) for 18 h with or without cysteine deprivation. Error bars, mean ± SEM; two-tailed t test, $^{***}p < 0.001$, n = 3 biological replicates.

accumulation in lysosomes attenuates cysteine stress response, thereby maximizing ferroptosis by inhibiting the adaptive ATF4 expression. Supporting this notion, silencing ATF4 sensitizes ferroptosis upon cysteine starvation (Figure S5L). Since AhR mediates ATF4 induction during cysteine response, we used AhR modulators to dissect the role of ATF4 in ferroptosis. Without disrupting the cysteine-to-cystine cycle, the AhR inhibitor SR1 promoted ferroptosis of cysteine-starved cells (Figure 4D). Strikingly, the AhR activator indirubin completely rescued the cells from ferroptosis with a marked reduction in lipid oxidation. Therefore, an increased ATF4 expression effectively counteracts ferroptosis, presumably via the increased X_c^- and enhanced antioxidant response.

Attenuated cysteine stress response sensitizes cancer cells to ferroptosis

Inducible ferroptosis has been harnessed for cancer therapy in recent years.[31] Common strategies for cysteine depletion include X_c^- inhibition or application of cysteine-degrading enzymes like cyst(e)inase, which have shown promising results by promoting tumor-selective ferroptosis.[32,33] However, the efficacy is compromised by rapid adaptation of cancer cells to cysteine limitation via induced ATF4 expression. Following the lead that a cystine accumulation in lysosomes potentiates ferroptosis, we hypothesized that a blockade of lysosomal cystine efflux by inactivating CTNS would maximize ferroptoic death of cancer cells. Notably, Kaplan-Meier plotter reveals that high expression of *CTNS* correlates with decreased overall survival of kidney, lung, and gastric cancer patients (Figure S6A), suggesting an oncogenic role for CTNS. Using a renal carcinoma cell line UMRC6 that has high levels of SLC7A11, we found that silencing either *SLC7A11* or *CTNS* potentiated ferroptosis upon cysteine withdrawal (Figures 5A and 5B). Remarkably, knocking down both *SLC7A11* and *CTNS* caused severe cell death of UMRC6 cells, which was further manifested by deficient colony formation in soft agar (Figures 5C and S6B). The tumor suppressive effect of *CTNS* silencing also holds true in another cell line 786-O despite the low basal levels of SLC7A11 (Figures S6C and S6D). To examine

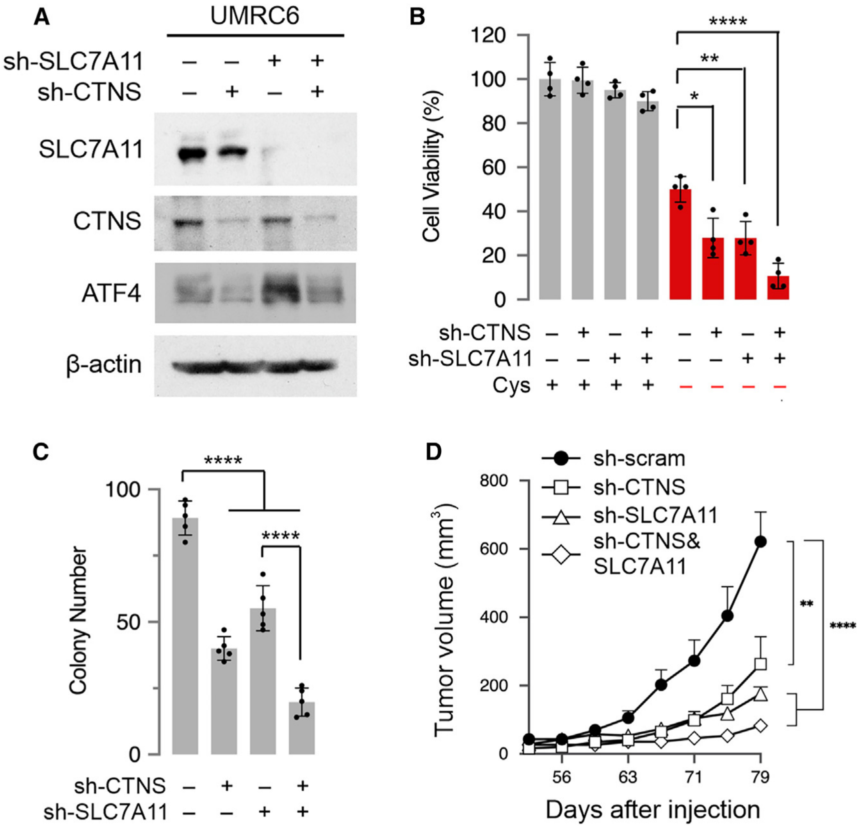

Figure 5. Attenuated cysteine stress response sensitizes cancer cells to ferroptosis

(A) Western blotting of UMRC6 cells subjected to CTNS and/or SLC7A11 knockdown.

(B) The cell viability in UMRC6 cells subjected to CTNS and/or SLC7A11 knockdown after 24 h cysteine deprivation. Error bars, mean ± SEM; two-tailed t test, $^{*}p < 0.05$, $^{**}p < 0.01$, $^{****}p < 0.0001$, n = 4 biological replicates.

(C) The bar graph shows the colony formation of UMRC6 cells subject to CTNS and/or SLC7A11 knockdown in soft agar. Error bars, mean ± SEM; two-tailed t test, $^{****}p < 0.0001$, n = 5 biological replicates.

(D) Tumor growth curves from UMRC6 cells subject to CTNS and/or SLC7A11 knockdown in SCID-beige mice after subcutaneous injection. Error bars, mean ± SEM; two-way ANOVA test, $^{**}p < 0.01$, $^{****}p < 0.0001$, n = 10 mice per group.

the role of CTNS in tumorigenesis *in vivo*, we conducted xenograft experiments using immuno-compromised severe combined immunodeficiency (SCID)-beige mice. Although silencing *SLC7A11* or *CTNS* suppressed UMRC6 tumor growth, knocking down both genes resulted in a nearly complete inhibition of tumorigenesis (Figure 5D).

Development of CysRx as a ferroptosis inducer

Despite the promising effect of *CTNS* silencing in promoting cancer cell ferroptosis, the encoded CTNS is crucial in maintaining lysosomal homeostasis.[34] Mutations in *CTNS* have been associated with cystinosis, a systemic disease with multiple clinical manifestations.[14] It is thus highly desirable to create an alternative way to block lysosomal cystine efflux without genetic perturbation. We reason that, by coupling translation of a cysteine-rich polypeptide and co-translational lysosome targeting, it is possible to direct cytosolic cysteine into the lysosome (Figure 6A). A survey of human coding sequences revealed many cysteine-rich domains in a large group of proteins. For instance, a cysteine-string protein (CSP) encoded by *DNAJC5* contains 15 cysteines within a stretch of 25 amino acids. Cysteine-rich tail 1 (CYSRT1) comprises a similar cysteine-rich motif with a stretch of 20 amino acids containing 12 cysteines. We fused both CSP and CYSRT1 motifs to insulin-like growth factor 2 (IGF2) to enable lysosomal targeting via the mannose-6-phosphate receptor (M6PR).[35] We named this fusion construct as a cyst(e)ine reverse exchanger (CysRx) because it converts cytosolic cysteine into lysosomal cystine (Figure 6B, top panel). Inspired by the recent success of mRNA vaccines,[36] we prepared synthetic mRNAs encoding CysRx for follow-up studies. Cell fractionation analysis confirmed lysosomal localization of CysRx (Figure 6B). Supporting lysosomal degradation of CysRx, BafA1 treatment resulted in CysRx accumulation. Importantly, CysRx-transfected cells showed a significant decrease of cytosolic cysteine and a corresponding increase of lysosomal cystine (Figure 6C). Mimicking CTNS knockdown, CysRx overexpression attenuated ATF4 expression in response to cysteine withdrawal (Figure 6D). As a result, cysteine-starved cells became more susceptible to ferroptosis (Figure 6E).

CysRx induces ferroptosis in cancer

We next transfected UMRC6 cells with CysRx mRNA, which sensitized cells to ferroptosis with significantly increased lipid oxidation (Figure 7A). By potently suppressing the adaptive ATF4 expression (Figure 7B), CysRx inhibited colony formation of UMRC6 in a dose-dependent manner (Figure 7C). The inhibitory role of CysRx in tumorigenesis was also observed in 786-O cells (Figure S7A), suggesting that the efficacy of CysRx is independent of SLC7A11. The CysRx-induced ferroptosis is not limited to renal carcinoma cells. Applying CysRx to a lung cancer cell line A549 not only reduced ATF4 expression (Figure S7B) but also promoted ferroptosis under cysteine starvation (Figure S7C).

To assess the therapeutic potential of CysRx *in vivo*, we formulated lipid nanoparticles using an ionizable lipid N^1,N^3,N^5-tris(2-aminoethyl)benzene-1,3,5-tricarboxamide derivatives (TT3) that enables efficient nucleic acid encapsulation, cellular delivery, and endosomal release[37] (Figure S7D). We also incorporated N^1-methylpseudouridine into the synthesized reporter mRNA that exhibited prolonged signals compared with the non-modified version in transfected UMRC6 cells (Figure S7E). We next evaluated the effect of CysRx-TT3 in the xenografted UMRC6 tumors via

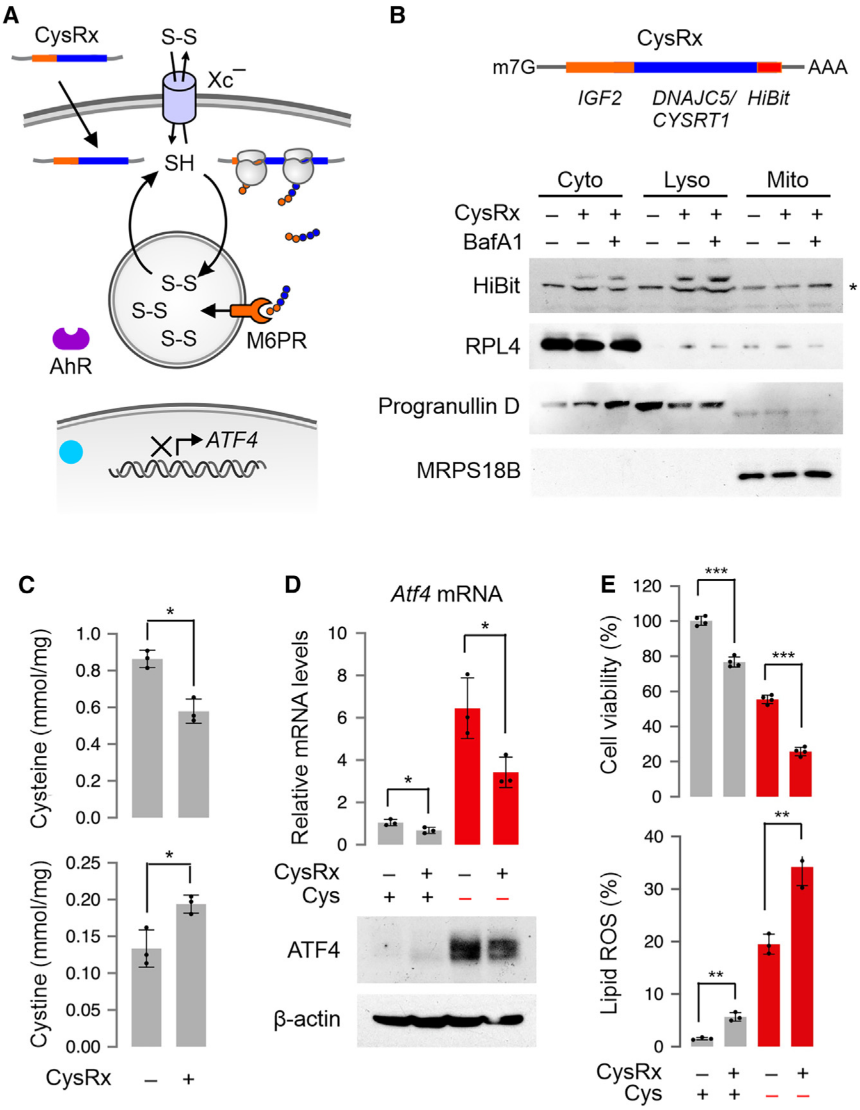

Figure 6. Development of CysRx

(A) Schematic of CysRx actions that convert cytosolic cysteine into lysosomal cystine.

(B) The top panel shows the schematic of CysRx design. The bottom panels show western blotting of fractionated MEF cells transfected with CysRx in the presence or absence of bafilomycin A (50 nM) for 12 h. Cell fractions are cytoplasmic (Cyto), lysosomal (Lyso), and mitochondria (Mito). *, non-specific bands.

(C) Total cysteine (top) and cystine (bottom) levels in MEF cells after 24 h of CysRx transfection (5 μg). Both measurements were normalized to protein levels. Error bars, mean ± SEM; two-tailed t test, $^{*}p < 0.05$, n = 3 biological replicates.

(D) The top bar graph shows the RT-qPCR results of *Atf4* (normalized to *Gapdh*) in MEF cells transfected with CysRx with or without 12 h of cysteine starvation. Error bars, mean ± SEM; two-tailed t test, $^{*}p < 0.05$, n = 3 biological replicates. The bottom panel shows the representative western blotting of ATF4 in transfected MEF cells.

(E) The left panel shows the cell viability in MEF cells transfected with CysRx with or without 12 h of cysteine starvation. Error bars, mean ± SEM; two-tailed t test, $^{***}p < 0.001$, n = 4 biological replicates. The right panel shows lipid ROS levels in transfected MEF cells. Error bars, mean ± SEM; two-tailed t test, $^{**}p < 0.01$, n = 3 biological replicates.

intratumor administration. Compared with the TT3 control expressing the nano-luciferase peptide HiBiT, CysRx-TT3 induced a significant delay in tumor progression after weekly injection (Figure 7D, left panel). Supporting enhanced ferroptotic cell death, tumors treated with CysRx-TT3 displayed significant accumulation of 4-hydroxynonenal (4HN), a by-product of lipid peroxidation (Figures S7F and S7G). The increased lipid oxidation was further confirmed by C11-BODIPY staining using isolated tumor samples (Figure S7H). The tumor suppressive effect of CysRx is partly due to the attenuated cysteine stress response as evidenced by the lowered ATF4 levels in isolated tumor samples (Figure S7I). We further tested the therapeutic potential of CysRx-TT3 in combination with the system X_c^- inhibitor imidazole ketone erastin (IKE). Similar to prior studies,[38] intraperitoneal administration of IKE (10 mg/kg) suppressed tumor growth. Intratumoral administration of CysRx-TT3 further reduced tumor growth with increased 4HN accumulation (Figures S7F, right panel and S7G), suggesting a synergistic effect in promoting ferroptotic cell death *in vivo*. Notably, systemic administration of IKE resulted in weight loss (Figure 7E), which was not evident in mice treated with CysRx-TT3. Therefore, CysRx holds therapeutic potential in cancer treatment by inducing ferroptosis.

DISCUSSION

Our work indicates that cysteine and cystine are not synonymous in metabolic regulation. Although cytosolic cysteine contributes to the synthesis of proteins and antioxidants, it is the lysosomal cystine that mediates the adaptive stress response. Upon cysteine withdrawal, the lysosomal cystine is mobilized via CTNS to mitigate cysteine shortage. This feature likely explains the insensitivity of cysteine to nutrient signaling pathways such as GCN2 and mTOR, despite the fact that cysteine is the least abundant amino acid inside cells.[11] Only when the lysosomal cystine efflux is blocked (e.g., by CTNS knockdown), does cysteine starvation inhibit global protein synthesis. Since many other amino acids (e.g., leucine) are potent regulators of mTOR, their shortage triggers robust general amino acid response. It is conceivable that full amino acid starvation compromises the unique cysteine stress response. Unlike the general amino acid response, the cysteine stress response is independent of the GCN2/eIF2α phosphorylation pathway. Previous studies reported similar findings in animals with sulfur amino acid restriction.[39] We demonstrate that cysteine stress response is characterized by transcriptional upregulation of ATF4. Acting as a master regulator of amino acid homeostasis, ATF4 protects cells from nutrient starvation by

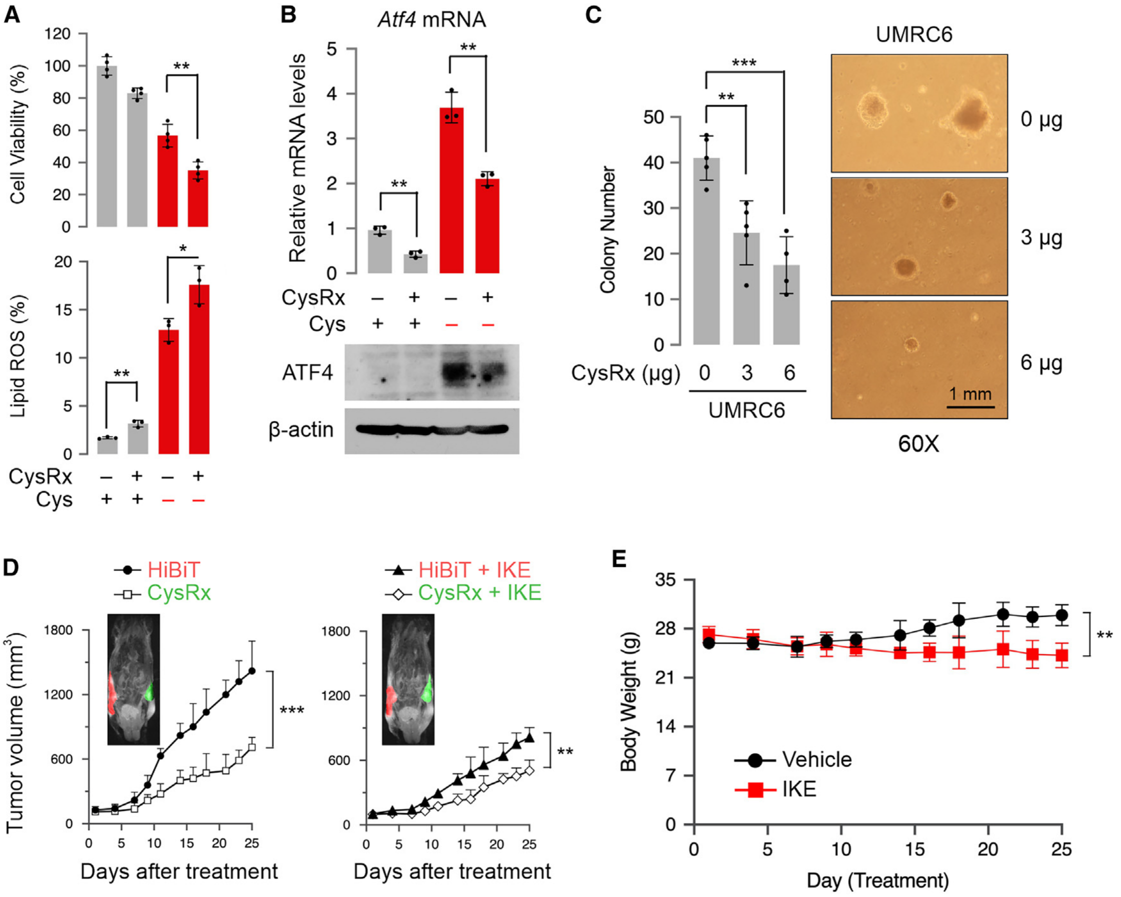

Figure 7. CysRx induces ferroptosis in cancer

(A) The top panel shows the cell viability in UMRC6 cells after 24 h of CysRx (5 μg) transfection with or without cysteine deprivation. Error bars, mean ± SEM; two-tailed t test, $^{**}p < 0.01$, n = 4 biological replicates. The bottom panel shows the lipid ROS levels in UMRC6 cells after 18 h of CysRx (5 μg) transfection with or without cysteine deprivation. Error bars, mean ± SEM; two-tailed t test, $^{*}p < 0.05$, $^{**}p < 0.01$, n = 3 biological replicates.

(B) The top bar graph shows the RT-qPCR results of *Atf4* (normalized to *Gapdh*) in UMRC6 cells after 12 h of CysRx (5 μg) transfection with or without cysteine deprivation. Error bars, mean ± SEM; two-tailed t test, $^{**}p < 0.01$, n = 3 biological replicates. The bottom panel shows the representative western blotting of ATF4 in UMRC6 cells after 12 h of CysRx (5 μg) transfection with or without cysteine deprivation.

(C) Quantified colony formation of UMRC6 cells transfected with CysRx treatment in soft agar. Error bars, mean ± SEM; two-tailed t test, $^{**}p < 0.01$, $^{***}p < 0.001$, n = 5 biological replicates. Images were taken 21 days post plating and treatment.

(D) Tumor growth curves from UMRC6 cells implanted bilaterally in SCID-beige mice. Mice were treated with IKE or vehicle control (10 mg/kg/2 days) for 25 days. CysRx or HiBiT mRNA (0.5 mg/kg/7 days) was intratumorally injected into each flank in the form of LNP. Representative magnetic resonance imaging (MRI) images are shown with tumors in green treated with CysRx-TT3 and tumors in red treated with HiBiT-TT3. Error bars, mean ± SEM; two-way ANOVA test, $^{**}p < 0.01$, $^{***}p < 0.001$, n = 6 mice per group.

(E) Body weight of SCID-beige mice treated with intraperitoneal administration of IKE (10 mg/kg/2 days) or equal volume of vehicle for the duration of the study. Error bars, mean ± SEM; two-tailed t test, $^{**}p < 0.01$, n = 6 mice per group.

regulating the expression of amino acid synthetic genes and their transporters to ensure a constant supply of nutrients.

Perhaps the most surprising finding is the lysosome-nucleus signaling pathway that mediates the cysteine stress response. We found that AhR, a member of the basic-helix-loop-helix superfamily of transcription factors, is activated upon lysosomal cystine depletion. AhR is known as a promiscuous receptor because of its propensity to bind to a variety of exogenous and endogenous ligands with different chemical characteristics.[30] Untargeted metabolomics revealed a hyperactivated kynurenine pathway in response to lysosomal cystine shortage. The kynurenine pathway is associated with tryptophan metabolism.[40] Previous studies reported that a tryptophan synthase from *Escherichia coli* catalyzes tryptophan biogenesis from indole and cysteine.[41] It is possible that lowered cystine drives tryptophan degradation in mammalian cells. Supporting this notion, untargeted metabolomics also uncovered many tryptophan byproducts such as 5-HIAA, ITE, and indirubin. Like kynurenine metabolites, many of those tryptophan products are potent AhR activators. Thus, the AhR signaling pathway senses a much broader range of intracellular metabolites, forming a new layer of lysosome-nucleus communication.

Cysteine is a potent regulator of ferroptosis, and many ferroptosis inducers interfere with cysteine metabolism. However, the role of lysosomal cystine has been largely overlooked. Since lysosomal cystine controls the cysteine stress response, the adaptive ATF4 induction is expected to counteract the inducible ferroptosis. This mechanism provides a potential explanation for why engineered cysteine-degrading enzyme cyst(e)inase has limited efficacy *in vivo* on tumor regression.[33] Of note, upregulated ATF4 enables tumor progression under adverse conditions.[42] To maximize ferroptosis in cancer, it is thus important to minimize the adaptive cysteine response. By promoting the cysteine-to-cystine cycle inside cells, it is possible to achieve cysteine depletion without inducing cysteine stress response. The development of CysRx not only confirms the regulatory role of lysosomal cystine in cysteine response but also provides a platform of mRNA engineering to starve cancer cells of specific amino acids without gross nutrient perturbation. As a result, CysRx acts as a cytosolic cysteine sponge and a lysosomal cystine dumpster. Although the former maximizes cysteine depletion, the latter blocks the adaptive cysteine response. Serving as a proof-of-principle, CysRx administration in the form of lipid nanoparticles effectively induced tumor ferroptosis *in vivo*. Given the broad function of AhR in immune responses,[30] we envision that CysRx offers a promising therapeutic approach to a wide range of human diseases via intracellular nutrient reprogramming.

Limitations of the study

Although lysosomal cystine shortage triggers transcriptional upregulation of ATF4 via the AhR signaling pathway, how exactly AhR senses cystine levels remains elusive. More specifically, how the kynurenine pathway responds to lysosomal metabolites warrants further investigation. Additionally, activating AhR alone is not sufficient to induce ATF4 expression under the normal growth condition, suggesting the existence of co-factors sensitive to cysteine deprivation. Identifying such co-factors in cysteine stress response will be one of our future endeavors. A recent study reported that different cancer cell lines have a wide range of cysteine sensitivities.[43] To generalize the concept that lysosomal cystine governs ferroptosis sensitivity in cancer, additional studies using different cancer cells are needed. The development of CysRx represents a prototype in achieving intracellular nutrient reprogramming. However, on-target delivery of CysRx will be highly desirable in future therapeutic applications. In coupling with tissue-specific nanolipid particles, we envision that CysRx holds the potential to selectively induce cancer cell ferroptosis *in vivo*.

STAR★METHODS

Detailed methods are provided in the online version of this paper and include the following:

- KEY RESOURCES TABLE
- RESOURCE AVAILABILITY
  - ○ Lead contact
  - ○ Materials availability
  - ○ Data and code availability
- EXPERIMENTAL MODEL AND STUDY PARTICIPANT DETAILS
  - ○ Cell lines
  - ○ Mouse strains
- METHOD DETAILS
  - ○ Antibodies
  - ○ Amino acid starvation
  - ○ Real-time quantitative PCR
  - ○ Lentiviral shRNAs
  - ○ siRNA transfection
  - ○ Immunoblotting
  - ○ Cysteine, cystine, and glutathione measurement
  - ○ Polysome profiling
  - ○ Puromycin labeling
  - ○ Luciferase reporter assay
  - ○ Cell viability assay
  - ○ Lipid peroxidation measurement
  - ○ Chromatin immunoprecipitation
  - ○ Untargeted metabolomics
  - ○ *In vitro* transcription
  - ○ Cell fractionation
  - ○ Colony formation on soft agar
  - ○ Formulation of mRNA-loaded TT3 lipid nanoparticles
  - ○ Xenotransplantation of UMRC6 cells
  - ○ CysRx treatment of UMRC6 tumors
  - ○ Magnetic resonance imaging of mice
  - ○ Immunohistochemistry
- QUANTIFICATION AND STATISTICAL ANALYSIS
  - ○ RNA-seq analysis

SUPPLEMENTAL INFORMATION

Supplemental information can be found online at https://doi.org/10.1016/j.molcel.2023.08.004.

ACKNOWLEDGMENTS

We are grateful to B. Gan, R. Wek, and R.J. Kaufman for sharing cell lines and plasmids. We thank Martha H. Stipanuk and Robert S. Weiss for their critical reading of our manuscript. We thank Cornell University Life Sciences Core Laboratory Center for sequencing and FACS and the Progressive Assessment of Therapeutics (PATh) Facility for mouse assistance. R.V.S. was supported by Chemical Biology Interface (CBI) training grant (T32GM008500) and AHA predoctoral fellowship (20PRE35210408). This work was supported by US National Institutes of Health (R01GM1222814 and DP1GM142101) and HHMI Faculty Scholar (55108556) to S.-B.Q.

AUTHOR CONTRIBUTIONS

S.-B.Q. conceived the project and designed the experiments. R.V.S. performed the majority of experiments. Q.J. contributed to the AhR ChIP analysis, imaging, and knockdown experiments. X.W. performed ATF4 silencing, RNA-seq, and all experiments during revision. L.D. contributed to the sequencing library construction. Y.M. and S.U. conducted the sequencing data analysis. J.Y. and Y.D. formulated TT3 LNP. S.-B.Q. wrote the manuscript. All authors initially discussed the results and edited the manuscript.

DECLARATION OF INTERESTS

S.-B.Q. is the co-founder of EzraBio Inc. S.-B.Q. and R.V.S. are inventors of CysRx with patent (PCT/US2022/073776) filed by Cornell University.

Received: October 28, 2022
Revised: May 22, 2023
Accepted: August 4, 2023
Published: August 29, 2023

REFERENCES

1. Wek, R.C., Jiang, H.Y., and Anthony, T.G. (2006). Coping with stress: eIF2 kinases and translational control. Biochem. Soc. Trans. *34*, 7–11. https://doi.org/10.1042/BST20060007.
2. Harding, H.P., Zhang, Y., Zeng, H., Novoa, I., Lu, P.D., Calfon, M., Sadri, N., Yun, C., Popko, B., Paules, R., et al. (2003). An integrated stress response regulates amino acid metabolism and resistance to oxidative stress. Mol. Cell *11*, 619–633. https://doi.org/10.1016/s1097-2765(03)00105-9.
3. Sonenberg, N., and Hinnebusch, A.G. (2007). New modes of translational control in development, behavior, and disease. Mol. Cell *28*, 721–729. https://doi.org/10.1016/j.molcel.2007.11.018.
4. Shu, X.E., Swanda, R.V., and Qian, S.B. (2020). Nutrient control of mRNA translation. Annu. Rev. Nutr. *40*, 51–75. https://doi.org/10.1146/annurev-nutr-120919-041411.
5. Ameri, K., and Harris, A.L. (2008). Activating transcription factor 4. Int. J. Biochem. Cell Biol. *40*, 14–21. https://doi.org/10.1016/j.biocel.2007.01.020.
6. Wortel, I.M.N., van der Meer, L.T., Kilberg, M.S., and van Leeuwen, F.N. (2017). Surviving stress: modulation of ATF4-mediated stress responses in normal and malignant cells. Trends Endocrinol. Metab. *28*, 794–806. https://doi.org/10.1016/j.tem.2017.07.003.
7. Hinnebusch, A.G. (2005). Translational regulation of GCN4 and the general amino acid control of yeast. Annu. Rev. Microbiol. *59*, 407–450. https://doi.org/10.1146/annurev.micro.59.031805.133833.
8. Vattem, K.M., and Wek, R.C. (2004). Reinitiation involving upstream ORFs regulates ATF4 mRNA translation in mammalian cells. Proc. Natl. Acad. Sci. USA *101*, 11269–11274. https://doi.org/10.1073/pnas.0400541101.
9. Stipanuk, M.H., Dominy, J.E., Jr., Lee, J.I., and Coloso, R.M. (2006). Mammalian cysteine metabolism: new insights into regulation of cysteine metabolism. J. Nutr. *136*. 1652S–1659S.
10. Conrad, M., and Sato, H. (2012). The oxidative stress-inducible cystine/glutamate antiporter, system x (c) (-): cystine supplier and beyond. Amino Acids *42*, 231–246. https://doi.org/10.1007/s00726-011-0867-5.
11. Poltorack, C.D., and Dixon, S.J. (2022). Understanding the role of cysteine in ferroptosis: progress & paradoxes. FEBS Journal *289*, 374–385. https://doi.org/10.1111/febs.15842.
12. Adelmann, C.H., Traunbauer, A.K., Chen, B., Condon, K.J., Chan, S.H., Kunchok, T., Lewis, C.A., and Sabatini, D.M. (2020). MFSD12 mediates the import of cysteine into melanosomes and lysosomes. Nature *588*, 699–704. https://doi.org/10.1038/s41586-020-2937-x.
13. Abu-Remaileh, M., Wyant, G.A., Kim, C., Laqtom, N.N., Abbasi, M., Chan, S.H., Freinkman, E., and Sabatini, D.M. (2017). Lysosomal metabolomics reveals V-ATPase- and mTOR-dependent regulation of amino acid efflux from lysosomes. Science *358*, 807–813. https://doi.org/10.1126/science.aan6298.
14. Gahl, W.A., Thoene, J.G., and Schneider, J.A. (2002). Cystinosis. N. Engl. J. Med. *347*, 111–121. https://doi.org/10.1056/NEJMra020552.
15. Dixon, S.J., Lemberg, K.M., Lamprecht, M.R., Skouta, R., Zaitsev, E.M., Gleason, C.E., Patel, D.N., Bauer, A.J., Cantley, A.M., Yang, W.S., et al. (2012). Ferroptosis: an iron-dependent form of nonapoptotic cell death. Cell *149*, 1060–1072. https://doi.org/10.1016/j.cell.2012.03.042.
16. Stockwell, B.R., Friedmann Angeli, J.P., Bayir, H., Bush, A.I., Conrad, M., Dixon, S.J., Fulda, S., Gascón, S., Hatzios, S.K., Kagan, V.E., et al. (2017). Ferroptosis: A regulated cell death nexus linking metabolism, redox Biology, and disease. Cell *171*, 273–285. https://doi.org/10.1016/j.cell.2017.09.021.
17. Zhang, Y., Swanda, R.V., Nie, L., Liu, X., Wang, C., Lee, H., Lei, G., Mao, C., Koppula, P., Cheng, W., et al. (2021). mTORC1 couples cyst(e)ine availability with GPX4 protein synthesis and ferroptosis regulation. Nat. Commun. *12*, 1589. https://doi.org/10.1038/s41467-021-21841-w.
18. Bersuker, K., Hendricks, J.M., Li, Z., Magtanong, L., Ford, B., Tang, P.H., Roberts, M.A., Tong, B., Maimone, T.J., Zoncu, R., et al. (2019). The CoQ oxidoreductase FSP1 acts parallel to GPX4 to inhibit ferroptosis. Nature *575*, 688–692. https://doi.org/10.1038/s41586-019-1705-2.
19. Doll, S., Freitas, F.P., Shah, R., Aldrovandi, M., da Silva, M.C., Ingold, I., Goya Grocin, A., Xavier da Silva, T.N., Panzilius, E., Scheel, C.H., et al. (2019). FSP1 is a glutathione-independent ferroptosis suppressor. Nature *575*, 693–698. https://doi.org/10.1038/s41586-019-1707-0.
20. Mao, C., Liu, X., Zhang, Y., Lei, G., Yan, Y., Lee, H., Koppula, P., Wu, S., Zhuang, L., Fang, B., et al. (2021). DHODH-mediated ferroptosis defence is a targetable vulnerability in cancer. Nature *593*, 586–590. https://doi.org/10.1038/s41586-021-03539-7.
21. Zhao, Q., Gao, S.M., and Wang, M.C. (2020). Molecular mechanisms of lysosome and nucleus communication. Trends Biochem. Sci. *45*, 978–991. https://doi.org/10.1016/j.tibs.2020.06.004.
22. Scheuner, D., Song, B., McEwen, E., Liu, C., Laybutt, R., Gillespie, P., Saunders, T., Bonner-Weir, S., and Kaufman, R.J. (2001). Translational control is required for the unfolded protein response and in vivo glucose homeostasis. Mol. Cell *7*, 1165–1176.
23. Kilberg, M.S., Shan, J., and Su, N. (2009). ATF4-dependent transcription mediates signaling of amino acid limitation. Trends Endocrinol. Metab. *20*, 436–443. https://doi.org/10.1016/j.tem.2009.05.008.
24. Conlon, M., Poltorack, C.D., Forcina, G.C., Armenta, D.A., Mallais, M., Perez, M.A., Wells, A., Kahanu, A., Magtanong, L., Watts, J.L., et al. (2021). A compendium of kinetic modulatory profiles identifies ferroptosis regulators. Nat. Chem. Biol. *17*, 665–674. https://doi.org/10.1038/s41589-021-00751-4.
25. Nguyen, T., Sherratt, P.J., Nioi, P., Yang, C.S., and Pickett, C.B. (2005). Nrf2 controls constitutive and inducible expression of ARE-driven genes through a dynamic pathway involving nucleocytoplasmic shuttling by Keap1. J. Biol. Chem. *280*, 32485–32492. https://doi.org/10.1074/jbc.M503074200.
26. Lange, P.S., Chavez, J.C., Pinto, J.T., Coppola, G., Sun, C.W., Townes, T.M., Geschwind, D.H., and Ratan, R.R. (2008). ATF4 is an oxidative stress-inducible, prodeath transcription factor in neurons in vitro and in vivo. J. Exp. Med. *205*, 1227–1242. https://doi.org/10.1084/jem.20071460.
27. Jézégou, A., Llinares, E., Anne, C., Kieffer-Jaquinod, S., O'Regan, S., Aupetit, J., Chabli, A., Sagné, C., Debacker, C., Chadefaux-Vekemans, B., et al. (2012). Heptahelical protein PQLC2 is a lysosomal cationic amino acid exporter underlying the action of cysteamine in cystinosis therapy. Proc. Natl. Acad. Sci. USA *109*. E3434–E3443. https://doi.org/10.1073/pnas.1211198109.
28. Schmidt, J.V., and Bradfield, C.A. (1996). Ah receptor signaling pathways. Annu. Rev. Cell Dev. Biol. *12*, 55–89. https://doi.org/10.1146/annurev.cellbio.12.1.55.
29. Denison, M.S., and Nagy, S.R. (2003). Activation of the aryl hydrocarbon receptor by structurally diverse exogenous and endogenous chemicals. Annu. Rev. Pharmacol. Toxicol. *43*, 309–334. https://doi.org/10.1146/annurev.pharmtox.43.100901.135828.
30. Rothhammer, V., and Quintana, F.J. (2019). The aryl hydrocarbon receptor: an environmental sensor integrating immune responses in health and disease. Nat. Rev. Immunol. *19*, 184–197. https://doi.org/10.1038/s41577-019-0125-8.
31. Chen, X., Kang, R., Kroemer, G., and Tang, D. (2021). Broadening horizons: the role of ferroptosis in cancer. Nat. Rev. Clin. Oncol. *18*, 280–296. https://doi.org/10.1038/s41571-020-00462-0.
32. Lim, J.K.M., Delaidelli, A., Minaker, S.W., Zhang, H.F., Colovic, M., Yang, H., Negri, G.L., von Karstedt, S., Lockwood, W.W., Schaffer, P., et al. (2019). Cystine/glutamate antiporter xCT (SLC7A11) facilitates oncogenic RAS transformation by preserving intracellular redox balance. Proc. Natl. Acad. Sci. USA *116*, 9433–9442. https://doi.org/10.1073/pnas.1821323116.
33. Badgley, M.A., Kremer, D.M., Maurer, H.C., DelGiorno, K.E., Lee, H.J., Purohit, V., Sagalovskiy, I.R., Ma, A., Kapilian, J., Firl, C.E.M., et al. (2020). Cysteine depletion induces pancreatic tumor ferroptosis in mice. Science *368*, 85–89. https://doi.org/10.1126/science.aaw9872.

34. Kalatzis, V., Cherqui, S., Antignac, C., and Gasnier, B. (2001). Cystinosin, the protein defective in cystinosis, is a H(+)-driven lysosomal cystine transporter. EMBO J. *20*, 5940–5949. https://doi.org/10.1093/emboj/20.21.5940.

35. Bochel, A.J., Williams, C., McCoy, A.J., Hoppe, H.J., Winter, A.J., Nicholls, R.D., Harlos, K., Jones, E.Y., Berger, I., Hassan, A.B., and Crump, M.P. (2020). Structure of the human cation-independent mannose 6-phosphate/IGF2 receptor Domains 7–11 uncovers the mannose 6-phosphate Binding Site of Domain 9. Structure *28*, 1300–1312.e5. https://doi.org/10.1016/j.str.2020.08.002.

36. Sahin, U., Muik, A., Derhovanessian, E., Vogler, I., Kranz, L.M., Vormehr, M., Baum, A., Pascal, K., Quandt, J., Maurus, D., et al. (2020). COVID-19 vaccine BNT162b1 elicits human antibody and TH1 T cell responses. Nature *586*, 594–599. https://doi.org/10.1038/s41586-020-2814-7.

37. Li, B., Luo, X., Deng, B., Wang, J., McComb, D.W., Shi, Y., Gaensler, K.M., Tan, X., Dunn, A.L., Kerlin, B.A., and Dong, Y. (2015). An orthogonal array optimization of lipid-like nanoparticles for mRNA delivery in vivo. Nano Lett. *15*, 8099–8107. https://doi.org/10.1021/acs.nanolett.5b03528.

38. Zhang, Y., Tan, H., Daniels, J.D., Zandkarimi, F., Liu, H., Brown, L.M., Uchida, K., O'Connor, O.A., and Stockwell, B.R. (2019). Imidazole ketone erastin induces ferroptosis and slows tumor growth in a mouse lymphoma model. Cell Chem. Biol. *26*, 623–633.e9. https://doi.org/10.1016/j.chembiol.2019.01.008.

39. Jonsson, W.O., Margolies, N.S., and Anthony, T.G. (2019). Dietary sulfur amino acid restriction and the integrated stress response: mechanistic insights. Nutrients *11*, 1349. https://doi.org/10.3390/nu11061349.

40. Badawy, A.A. (2017). Kynurenine pathway of tryptophan metabolism: regulatory and functional aspects. Int. J. Tryptophan Res. *10*, 1178646917691938. https://doi.org/10.1177/1178646917691938.

41. Newton, W.A., and Snell, E.E. (1964). Catalytic properties of tryptophanase, a multifunctional pyridoxal phosphate enzyme. Proc. Natl. Acad. Sci. USA *51*, 382–389. https://doi.org/10.1073/pnas.51.3.382.

42. Tameire, F., Verginadis, I.I., Leli, N.M., Polte, C., Conn, C.S., Ojha, R., Salas Salinas, C., Chinga, F., Monroy, A.M., Fu, W., et al. (2019). ATF4 couples MYC-dependent translational activity to bioenergetic demands during tumour progression. Nat. Cell Biol. *21*, 889–899. https://doi.org/10.1038/s41556-019-0347-9.

43. Zhang, T., Bauer, C., Newman, A.C., Uribe, A.H., Athineos, D., Blyth, K., and Maddocks, O.D.K. (2020). Polyamine pathway activity promotes cysteine essentiality in cancer cells. Nat. Metab. *2*, 1062–1076. https://doi.org/10.1038/s42255-020-0253-2.

44. Love, M.I., Huber, W., and Anders, S. (2014). Moderated estimation of fold change and dispersion for RNA-seq data with DESeq2. Genome Biol. *15*, 550. https://doi.org/10.1186/s13059-014-0550-8.

45. Dobin, A., Davis, C.A., Schlesinger, F., Drenkow, J., Zaleski, C., Jha, S., Batut, P., Chaisson, M., and Gingeras, T.R. (2013). STAR: ultrafast universal RNA-seq aligner. Bioinformatics *29*, 15–21. https://doi.org/10.1093/bioinformatics/bts635.

46. Langmead, B., Trapnell, C., Pop, M., and Salzberg, S.L. (2009). Ultrafast and memory-efficient alignment of short DNA sequences to the human genome. Genome Biol. *10*, R25. https://doi.org/10.1186/gb-2009-10-3-r25.

47. Robinson, M.D., McCarthy, D.J., and Smyth, G.K. (2010). edgeR: a Bioconductor package for differential expression analysis of digital gene expression data. Bioinformatics *26*, 139–140. https://doi.org/10.1093/bioinformatics/btp616.

48. Zhang, W., Li, P., Geng, Q., Duan, Y., Guo, M., and Cao, Y. (2014). Simultaneous determination of glutathione, cysteine, homocysteine, and cysteinylglycine in biological fluids by ion-pairing high-performance liquid chromatography coupled with precolumn derivatization. J. Agric. Food Chem. *62*, 5845–5852. https://doi.org/10.1021/jf5014007.

49. Campanella, L., Crescentini, G., and Avino, P. (1999). Simultaneous determination of cysteine, cystine and 18 other amino acids in various matrices by high-performance liquid chromatography. J. Chromatogr. A *833*, 137–145. https://doi.org/10.1016/s0021-9673(98)01023-1.

50. Schmidt, E.K., Clavarino, G., Ceppi, M., and Pierre, P. (2009). SUnSET, a nonradioactive method to monitor protein synthesis. Nat. Methods *6*, 275–277. https://doi.org/10.1038/nmeth.1314.

51. The RNAcentral Consortium (2019). RNAcentral: a hub of information for non-coding RNA sequences. Nucleic Acids Res. *47*. D221–D229. https://doi.org/10.1093/nar/gky1034.

STAR★METHODS

KEY RESOURCES TABLE

REAGENT or RESOURCE	SOURCE	IDENTIFIER
Antibodies		
ATF4 Antibody	Cell Signaling Technology	11815S; RRID: AB_2616025
P-eIF2α Antibody	Cell Signaling Technology	3398S; RRID: AB_2096481
eIF2α Antibody	Cell Signaling Technology	5324S; RRID: AB_10692650
β-Actin Antibody	Sigma-Aldrich	A5441; RRID: AB_476744
Slc7a11 Antibody	Abcam	ab37185; RRID: AB_778944
Nrf2 Antibody	Santa Cruz Biotechnology	sc-365949; RRID: AB_10917561
Cystinosin Antibody	Aviva Systems Biology	ARP44766_P050;
GCN2 Antibody	Cell Signaling Technology	3302S; RRID: AB_2277617
Rpl4 Antibody	Proteintech	11302-1-AP; RRID: AB_2181909
Progranulin D Antibody	R&D Systems	AF2557; RRID: AB_2114504
Mrps18b Antibody	Proteintech	16139-1-AP; RRID: AB_2146368
HSP90 Antibody	Cell Signaling Technology	8165S; RRID: AB_11217436
4HNE	Abcam	ab46545; RRID: AB_722490
Bacterial and virus strains		
DECIPHER pRSI9-U6-(sh)-UbiC-TagRFP-2A-Puro	Cellecta	N/A
Subcloning Efficiency DH5a Competent Cells	Invitrogen	Cat#18265-017
Chemicals, peptides, and recombinant proteins		
MEM Non-Essential Amino Acids Solution	Invitrogen	11140050
Cycloheximide	Sigma Aldrich	C7698-5G
Puromycin	Sigma Aldrich	P7255-250MG
Bafilomycin A	Sigma Aldrich	B1793
Concanamycin A	Sigma Aldrich	C9705
Cysteamine	Sigma Aldrich	M9768
SR1	Sigma Aldrich	182706
Indirubin	Sigma Aldrich	SML0280
Erastin	Sigma Aldrich	E7781
Sulfasalazine	Sigma Aldrich	S0883
Z-VAD-fmk	Invivogen	tlrl-vad
Necrostatin-1	Santa-Cruz Biotechnology	sc-200142
Ferrostatin-1	Sigma Aldrich	SML0583
L-buthionine-sulfoximine	Sigma Aldrich	B2515
10% dialyzed FBS	Sigma Aldrich	F0392
HBSS buffer	Lonza (VWR)	10-527F
TRIzol	Invitrogen	15596-018
Power SYBR Green PCR Master Mix	Applied Biosystems	4368706
Lipofectamine 2000	Invitrogen	11668-019
Triton-X100	Millipore Sigma	T8787-100mL
TURBO DNase	Thermo Fisher Scientific	AM1907
DL-Dithiothreitol	Sigma Aldrich	D0632-5G
BSA	Sigma-Aldrich	A3803-100G
Tween-20	Sigma-Aldrich	P1379-100ML

(*Continued on next page*)

Continued

REAGENT or RESOURCE	SOURCE	IDENTIFIER
Pierce™ Protease Inhibitor Tablets, EDTA-free	Thermo Fisher Scientific	A32965
Tris(2-carboxyethyl) phosphine hydrochloride	Sigma-Aldrich	C4706-2G
4-chlorro-3,5- dinitrobenzotrifluorride	Sigma-Aldrich	197017
5-Sulfosalicylic Acid Dyhydrate solution	Sigma-Aldrich	S3147
Trifluoroacetic acid (TFA)	Oakwood Chemical	001271-1L
Sucrose	Thermo Fisher Scientific	BP220-212
Blotting-Grade Blocker	Bio-Rad	1706404
BODIPY 581/591 C11 dye	Invitrogen	D3861
Formamide	Sigma-Aldrich	F9037
IGEPAL® CA-630	Sigma-Aldrich	I8896
N1-methylpseudouridine (Ψ)	APExBIO	B8049
Lithium chloride	Sigma-Aldrich	L9650
TT3	Dr. Yizhou Dong	N/A
2-dioleoyl-sn-glycero-3-phosphoethanolamine (DOPE)	Sigma-Aldrich	76548-100MG
Methoxypolyethylene glycol (DMG-PEG2000)	Avanti Polar Lipids	880151
Cholesterol	Sigma-Aldrich	C8667-1G
1,2-dimyristoyl-snglycerol	Cayman Chemicals	15077
O.C.T.	Tissue-Teck	4583
hematoxylin	Thermo Fisher Scientific	CS401-1D
Critical commercial assays		
Dual-Luciferase Reporter Assay System	Promega	E1910
CellTiter-Blue viability assay	Promega	G8081
mMESSAGE mMACHINE T7 Transcription Kit	Invitrogen	AM1344
Poly(A) Tailing Kit	Invitrogen	AM1350
Nano-Glo HiBiT Blotting System	Promega	N2410
High-Capacity cDNA Reverse Transcription Kit	Invitrogen	4368814
Protein Assay kit	Bio-Rad	5000112
Lysosome isolation kit	Thermo Fisher Scientific	89839
Rabbit specific HRP/DAB (ABC) Detection IHC Kit (ab64261)	Abcam	ab64261
Deposited data		
Raw Image	This paper	https://doi.org/10.17632/b4wd64nzk3.1
RNA-seq	GEO	accession number, GSE237928
Experimental models: Cell lines		
MEF	Laboratory of David J. Kwiatkowski	N/A
HEK293	Laboratory of Jonathan Yewdell	N/A
UMRC6	Laboratory of Boyi Gan	N/A
786-O	N/A	N/A
MDA-MB-231	Laboratory of Robert Weiss	N/A
B16F10	Laboratory of Shaoyi Jiang	N/A
A549	Laboratory of John Parker	N/A
Lenti-X 293T	Takara Bio	632180
AT-3	Laboratory of Robert Weiss	N/A

(*Continued on next page*)

Continued

REAGENT or RESOURCE	SOURCE	IDENTIFIER
Experimental models: Organisms/strains		
Mouse: **NOD.Cg-*Prkdc*^{scid} *Il2rg*^{tm1Wjl}/SzJ**	The Jackson Laboratory	Cat#005557
Oligonucleotides		
Atf4 (mouse) forward primer for qPCR: CTTGATGTCCCCCTTCGACC	IDT	N/A
Atf4 (mouse) reverse primer for qPCR: CTTGTCGCTGGAGAACCCAT	IDT	N/A
Nrf2 (mouse) forward primer for qPCR: CCTCGCTGGAAAAAGAAGTG	IDT	N/A
Nrf2 (mouse) reverse primer for qPCR: GGAGAGGATGCTGCTGAAAG	IDT	N/A
Slc7a11 (mouse) forward primer for qPCR: GGCACCGTCATCGGATCAG	IDT	N/A
Slc7a11 (mouse) reverse primer for qPCR: CTCCACAGGCAGACCAGAAAA	IDT	N/A
Gapdh (mouse) forward primer for qPCR: CAAGGAGTAAGAAACCCTGGAC	IDT	N/A
Gapdh (mouse) reverse primer for qPCR: GGATGGAAATTGTGAGGGAGAT	IDT	N/A
Atf4 (human) forward primer for qPCR: TCAGTCCCTCCAACAACAGC	IDT	N/A
Atf4 (human) reverse primer for qPCR: TCTGGCATGGTTTCCAGGTC	IDT	N/A
Actin (human) forward primer for qPCR: AGATGTGGATCAGCAAGC	IDT	N/A
Actin (human) reverse primer for qPCR: TCATCTTGTTTTCTGCGC	IDT	N/A
AhR CHIP (mouse) forward primer for qPCR: ACAAGAGATGGCAGGTGTGA	IDT	N/A
AhR CHIP (mouse) reverse primer for qPCR: CTTGTCGCTGGAGAACCCAT	IDT	N/A
CTNS shRNA primer #1 (mouse): ACCGGGGAGGAATTGGCTGCTTATTTCTCGAGAAATAAGCAGCCAATTCCTCCTTTTTTG	IDT	N/A
CTNS shRNA primer #1 (mouse): CGAACAAAAAAGGAGGAATTGGCTGCTTATTTCTCGAGAAATAAGCAGCCAATTCCTCCC	IDT	N/A
CTNS shRNA primer #2 (mouse): ACCGGCCCTTGGGCATCCACTAAATTCTCGAGAATTTAGTGGATGCCCAAGGGTTTTTTG	IDT	N/A
CTNS shRNA primer #2 (mouse): CGAACAAAAAACCCTTGGGCATCCACTAAATTCTCGAGAATTTAGTGGATGCCCAAGGGC	IDT	N/A
CTNS shRNA primer #1 (human): ACCGGCAGTCACGCTGGTCAAGTATTCTCGAGAATACTTGACCAGCGTGACTGTTTTTTG	IDT	N/A
CTNS shRNA primer #1 (human): CGAACAAAAAACAGTCACGCTGGTCAAGTATTCTCGAGAATACTTGACCAGCGTGACTGC	IDT	N/A
Slc7a11 shRNA primer #1 (mouse): ACCGGGCAGGCGGTACCGAATCAGCCTCGAGGCTGATTCGGTACCGCCTGCTTTTTTG	IDT	N/A

(*Continued on next page*)

Continued

REAGENT or RESOURCE	SOURCE	IDENTIFIER
Slc7a11 shRNA primer #1 (mouse): CGAACAAAAAAGCAGGCGGTACCGAATCAGCCTCGAGGCTGATTCGGTACCGCCTGCC	IDT	N/A
Slc7a11 shRNA primer #2 (mouse): ACCGGGAGGGAAACTAAAAATGGAGCTCGAGCTCCATTTTTAGTTTCCCTCTTTTTTG	IDT	N/A
Slc7a11 shRNA primer #2 (mouse): CGAACAAAAAAGAGGGAAACTAAAAATGGAGCTCGAGCTCCATTTTTAGTTTCCCTCC	IDT	N/A
Slc7a11 shRNA primer #1 (human): ACCGGGGTGTTTCTGAGTAGTAATTACTCGAGTAATTACTACTCAGAAACACCTTTTTTG	IDT	N/A
Slc7a11 shRNA primer #1 (human): CGAACAAAAAAGGTGTTTCTGAGTAGTAATTACTCGAGTAATTACTACTCAGAAACACCC	IDT	N/A
AhR shRNA primer #1 (mouse): ACCGGTGAGGTGCCTGCTGGATAATTCTCGAGAATTATCCAGCAGGCACCTCATTTTTTG	IDT	N/A
AhR shRNA primer #1 (mouse): CGAACAAAAAATGAGGTGCCTGCTGGATAATTCTCGAGAATTATCCAGCAGGCACCTCAC	IDT	N/A
AhR shRNA primer #2 (mouse): ACCGGCAGAGCTCTTTCCGGATAATACTCGAGTATTATCCGGAAAGAGCTCTGTTTTTTG	IDT	N/A
AhR shRNA primer #2 (mouse): CGAACAAAAAACAGAGCTCTTTCCGGATAATACTCGAGTATTATCCGGAAAGAGCTCTGC	IDT	N/A
pAtf4 (-1200bp) F: ATTGACTAGTACGCCTGGGCCAATCAGCTCGAC	IDT	N/A
pAtf4 (-1000bp) F: ATTGACTAGTTCTCATGGGGCCTTTAGGACGAT	IDT	N/A
pAtf4 (-800bp) F: ATTGACTAGTCATTTCTGCTTGCTGTCTGCCGG	IDT	N/A
pAtf4 (-500bp) F: ATTGACTAGTGCGTTGCCTGCGACGCCGGCGCT	IDT	N/A
pAtf4 (-400bp) F: ATTGACTAGTGCTCACCGGGGTCCCCGTGTCAT	IDT	N/A
pAtf4 (-300bp) F: ATTGACTAGTCGTATTAGGACGCGAGGACAAGC	IDT	N/A
pAtf4 (-200bp) F: ATTGACTAGTCACAATGGCCTTGGGCCCGCGTG	IDT	N/A
pAtf4 (-100bp) F: ATTGACTAGTCCATCCAGGCTCTTCACGAAATC	IDT	N/A
pAtf4 (-400bp) R: ATGCGGATCCCCCGAGATGATTAAGCTAAGACA	IDT	N/A
pAtf4 (-800bp) R: ATGCGGATCCGGCGGCGGCACGCCCTAAACCCG	IDT	N/A
pAtf4 (-1000bp) R: ATGCGGATCCAGAAAAGTGCACTACTTTATAGG	IDT	N/A
pAtf4 (0bp) R: ATGCGGATCCGTTGTGGGGCTTTGCTGGATTCGAG	IDT	N/A
Recombinant DNA		
pLJM1-Tmem192-mRFP-3xHA	Addgene	134631
Firefly luciferase (pcDNA3.1)	This study	N/A

(*Continued on next page*)

Continued

REAGENT or RESOURCE	SOURCE	IDENTIFIER
Software and algorithms		
Prism 9 version 9.2.0	GraphPad	https://www.graphpad.com/scientificsoftware/prism/
FlowJo v10.7	BD Biosciences	https://www.flowjo.com/solutions/flowjo
R	The R Project for Statistical Computing	https://www.r-project.org/
Perl	Perl	https://www.perl.org/
Compound Discoverer 3.1	Thermo Fisher Scientific	https://thermofisher.com
DESeq2	Love et al.[44]	https://bioconductor.org/packages/release/bioc/html/DESeq2.html
ImageJ	NIH	https://imagej.nih.gov/ij/
Docker 25.0.5	Docker	https://www.docker.com/
Python 3.9	Python	https://www.python.org/
STAR 2.7.10a	Dobin et al.[45]	https://github.com/alexdobin/STAR
Bowtie 1.2.3	Langmead et al.[46]	https://bowtie-bio.sourceforge.net/
Cutadapt 2.8	Cutadapt	https://cutadapt.readthedocs.io/en/stable/
edgeR 3.40.1	Robinson et al.[47]	https://doi.org/10.18129/B9.bioc.edgeR
Custom Code	This study	https://doi.org/10.5281/zenodo.8197060

RESOURCE AVAILABILITY

Lead contact

All material request should be directed to Shu-Bing Qian (sq38@cornell.edu).

Materials availability

Reagents and materials produced in this study are available from the lead contact pending a completed Materials Transfer Agreement.

Data and code availability

- All Sequencing data are available in the Gene Expression Omnibus database (accession number, GSE237928). All raw images are available in Mendeley data. All data are publicly available as of the date of publication. Accession numbers and DOI are listed in the key resources table.
- All custom code has been deposited to GitHub and Zenodo. DOI are listed in the key resources table.
- Any additional information required to reanalyze the data reported in this paper is available from the lead contact upon request.

EXPERIMENTAL MODEL AND STUDY PARTICIPANT DETAILS

Cell lines

MEF cells, HEK293, UMRC6, 786-O, MDA-MB-231, A549, B16F10, and AT3 cells were maintained in Dulbecco's Modified Eagle's Medium (DMEM) with 10% fetal bovine serum (FBS). eIF2α(S/S) & eIF2α(A/A) MEFs were additionally supplemented with 5% non-essential amino acids (Invitrogen: 11140-050). All cells were grown at 37°C with 5% CO_2.

Mouse strains

NOD.Cg-*Prkdc*^{scid} *Il2rg*^{tm1Wjl}/SzJ, NSG, mice catalog number 005557 were sourced from The Jackson Laboratory and bred in house (Cornell University, USA) with the supervision of the Center for Animal Resources and Education (CARE) breeding program. All animals used in this study were handled in accordance with federal and institutional guidelines, under a protocol approved by the Cornell University Institutional Animal Care and Use Committee, protocol 2017-0035. Mice were housed under specific pathogen-free conditions in an Association for the Assessment and Accreditation of Laboratory Animal Care International-accredited facility and cared for in compliance with the Guide for the Care and Use of Laboratory Animals.

METHOD DETAILS

Antibodies

The following reagents were used at their indicated experimental concentrations and time points; cycloheximide (Sigma Aldrich: C7698-5G), puromycin (Sigma Aldrich: P7255-250MG), bafilomycinA (Sigma Aldrich: B1793), concanamycinA (Sigma Aldrich: C9705), cysteamine (Sigma Aldrich: M9768), SR1 (Sigma Aldrich: 182706), indirubin (Sigma Aldrich: SML0280), erastin (Sigma Aldrich: E7781), sulfasalazine (Sigma Aldrich: S0883), Z-VAD-fmk (Invivogen: tlrl-vad), necrostatin-1 (Santa-Cruz Biotechnology: sc-200142), ferrostatin-1 (Sigma Aldrich: SML0583), L-buthionine-sulfoximine (Sigma Aldrich: B2515). Antibodies are listed below: ATF4 (Cell Signaling: 11815S), P-eIF2α (Cell Signaling: 3398S), eIF2α (Cell Signaling: 5324S), β-Actin (Sigma: A5441), Slc7a11 (Abcam: ab37185), Nrf2 (Santa Cruz: sc-365949), Cystinosin (Aviva Systems Biology: ARP44766_P050), GCN2 (Cell Signaling: 3302S), HiBit (Promega: N2410), Rpl4 (Proteintech: 11302-1), Progranulin D (R&D Systems: AF2557), Mrps18b (Proteintech: 16139-1), HSP90 (Cell Signaling: 8165S).

Amino acid starvation

For cystine and methionine deprivation, the experiment was carried out by incubating cells in DMEM, high glucose, no glutamine, no methionine, no cysteine (Thermo Fisher: 21013024) with 10% dialyzed FBS (Sigma Aldrich: F0392). For leucine, histidine, and arginine deprivation, the experiment was carried out by incubating cells in DMEM, high glucose, no arginine, no histidine, no leucine, respectively, (custom prepared by Gibco/Invitrogen) with 10% dialyzed FBS (Sigma Aldrich: F0392). For full amino acid starvation, the experiment was carried out by incubating cells in HBSS buffer (Lonza) with 10% dialyzed FBS (Sigma Aldrich: F0392). Samples were collected at indicated experimental time points.

Real-time quantitative PCR

Following experimental conditions, total RNA was isolated by TRIzol reagent (Invitrogen) and reverse transcription was performed using High-Capacity cDNA Reverse Transcription Kit (Invitrogen). Real-time PCR analysis was conducted using Power SYBR Green PCR Master Mix (Applied Biosystems) and data was generated using a LightCycler 480 Real-Time PCR System (Roche Applied Science). qPCR oligo sequences are listed in key resources table.

Lentiviral shRNAs

All shRNA targeting sequences were cloned into DECIPHER pRSI9-U6-(sh)-UbiC-TagRFP-2A-Puro (Cellecta, CA). shRNA targeting sequences listed below were based on RNAi consortium at the Broad Institute (https://www.broad.mit.edu/rnai/trc). Lentiviral particles were packaged using Lenti-X 293T cells (Clontech) grown in DMEM media. Virus-containing supernatants were collected at 48 hrs post transfection and filtered with Millex-HA Syringe Filter Unit, 0.45 μm (Millipore) to eliminate any debris. Cells were infected with the lentivirus for 48 hrs before selection by 2 mg/mL puromycin. shRNA oligos are listed in key resources table.

siRNA transfection

siRNAs targeting mouse *Nrf2* (Santa Cruz: sc-37049) or scramble control (Santa Cruz: sc-37007) were transfected into MEF cells using Lipofectamine 2000 (Invitrogen) according to the manufacturer's instruction. Knockdown efficiency was examined 48 hrs after siRNA administration.

Immunoblotting

Cells were washed with PBS (Gibco) and then lysed on ice using cell lysis buffer (50 mM Tris [pH7.5], 150 mM NaCl, 1 mM EDTA, 1% Triton X-100, 2 U/ml DNase and protease inhibitor cocktail tablet). The lysates were incubated on ice for 30 min and spun down at 10,000 rpm for 3 mins to collect supernatant. Collected supernatant was measured by protein assay (Bio-Rad: 500-0112) to quantify the protein concentration. Equal amount of proteins across samples were mixed with SDS-PAGE sample buffer (50 mM Tris [pH6.8], 100 mM dithiothreitol, 2% SDS, 0.1% bromophenol blue, 10% glycerol) and heated for 9 mins at 95°C. Denatured proteins were separated on SDS-PAGE and transferred to PVDF membranes (Fisher). Membranes were blocked in TBS containing 5% non-fat milk and 0.1% Tween-20 for 1 hr. Phospho-proteins were blocked in TBS containing 5% BSA and 0.1% Tween-20 for 1 hr. Blocking was followed by incubation with primary antibodies overnight at 4°C. Membranes were washed using TBST followed by subsequent incubation using horseradish peroxidase-coupled secondary antibodies at room temperature for 1 hr. Immunoblots were washed again using TBST and visualized using enhanced chemiluminescence (ECL- Plus, GE Healthcare).

Cysteine, cystine, and glutathione measurement

Intracellular cysteine and glutathione levels were measured by methods described previously[48] with optimization. Cells were grown on 100 mm dishes until 80%–90% confluent. Cells were lysed on ice in lysis buffer (50 mM Tris [pH7.5], 150 mM NaCl, 1 mM EDTA, 1% Triton X-100, 2 U/ml DNase and protease inhibitor cocktail tablet), followed by centrifugation at 10,000 rpm for 8 min at 4°C. The supernatant was collected and 100 μL of sample was mixed with 10μL TCEP (50 mM in borate buffer [pH 7.4]) (Sigma Aldrich) in a vial and incubated at 25°C for 10 min. 90μL of a solution containing 1% TCA and 1 mM EDTA was then added. The total solution was centrifuged for 10 min at 10,000g at 4°C. 100μL of the obtained supernatant, 20μL of 10 mM CNBF solution (4-chlorro-3,5- dinitrobenzotrifluorride

[Sigma Aldrich: 197017]), 20μL of methanol, and 50μL of borate buffer (0.2 M [pH 8.0])) were mixed and incubated at 25°C for 20 min. Derivatization was terminated with 10μL of 2M HCl followed by HPLC analysis (see below).

Intracellular cystine was measured as described previously[49] with optimization. Cells were grown on 100 mm dishes until 80%–90% confluent. Cells were lysed on ice in lysis buffer (50 mM Tris [pH7.5], 150 mM NaCl, 1 mM EDTA, 1% Triton X-100, 2 U/ml DNase and protease inhibitor cocktail tablet). 100 μL of sample was mixed with 100 μL of 6% 5-Sulfosalicylic Acid Dyhydrate solution (Sigma: S3147), followed by centrifugation at 3,000g for 15 min at 4°C. The supernatant was collected and 25 μL of freshly made derivatizing solution was added. Samples sat at room temperature for 20 mins, followed by rotary evaporation. Dried material was dissolved in 150 μL of phase A solution followed by HPLC analysis (see below).

All resulting solutions for cysteine, glutathione, and cystine were filtered through a 0.22 μm filter membrane (Millipore Corporation, Belfast, MA, USA) and injected into a chromatographic system. High performance liquid chromatography (HPLC) was performed using a LC-20AT pump with a SPD-20AV UV-vis detector monitored at 270 and 220 nm (Shimadzu, Japan) equip with an Ultra Aqueous C18 column (100 Å, 5 μm, 250 mm × 4.6 mm; Restek, USA) at a flow rate of 1 mL/min with a mobile phase containing 0.1% trifluoroacetic acid (TFA) in H_2O or acetonitrile. Values were normalized to protein concentration by Bradford assay.

Polysome profiling

15% and 45% sucrose solutions were freshly prepared using polysome buffer (10 mM HEPES [pH 7.4], 100 mM KCl, 5 mM $MgCl_2$, 100 mg/ml cycloheximide, 2% Triton X-100) and loaded into SW41 ultracentrifuge tubes (Beckman). A 15%-45% density gradient was made using a Gradient Master (BioComp Instruments). Following experimental conditions, cells were washed using ice-cold PBS three times and then lysed in polysome lysis buffer (polysome buffer, 100 mg/ml cycloheximide, 10% Triton X-100). Cell debris were removed by centrifugation at 14,000 rpm for 10 min at 4°C. 500μL of supernatant was loaded onto the sucrose gradient followed by ultra-centrifugation for 2 hr 30 min at 35,000 rpm at 4°C in a SW41 rotor. Separated samples were fractionated at 0.75 ml/min through an automated fractionation system (Isco) that continually monitors OD254 values.

Puromycin labeling

Puromycin labeling was performed as previously described[50] with some modifications. Cells were grown to 70%–80% confluence and treated with puromycin (10 μg/ml) for 10 min. Cells were washed twice with ice-cold PBS, and then lysed on ice using cell lysis buffer (50 mM Tris [pH7.5], 150 mM NaCl, 1 mM EDTA, 1% Triton X-100, 2 U/ml DNase and protease inhibitor cocktail tablet). The lysates were incubated on ice for 30 min and spun down at 10,000 rpm for 3 mins to collect supernatant. Collected supernatant was followed by protein assay to measure protein concentration. Equal amount of proteins across samples were mixed with SDS-PAGE sample buffer (50 mM Tris [pH6.8], 100 mM dithiothreitol, 2% SDS, 0.1% bromophenol blue, 10% glycerol) and heated for 9 mins at 95°C. Denatured proteins were separated on a 10% SDS-PAGE gel and transferred to Immobilon-P membranes. Membranes were blocked for 1 hr in TBS containing 5% nonfat milk and 0.1% Tween 20, followed by incubation with puromycin antibodies (1:100 dilution) overnight at 4°C. The membrane was then washed with TBST and incubated with HRP-conjugated anti-mouse immunoglobulin G (IgG) (1:5000 dilution) for 1 hr at room temperature, followed by TBST wash and visualization using enhanced chemiluminescence.

Luciferase reporter assay

Firefly luciferase reporters were co-transfected with a Renilla reporter plasmid into MEF cells or *CTNS* knockdown cells for 4 hrs. Transfected cells were treated with amino acid starvation and/or compound treatment at indicated timepoints. Firefly and Renilla luciferase activities were measured using Dual-Luciferase Reporter Assay System (Promega). Relative values of firefly luciferase activities were normalized to Renilla luciferase control. Oligo sequences used for construction of truncated *Atf4* promoter regions are listed in the STAR Methods.

Cell viability assay

Cells were seeded into 96-well plates at 3,000 cells per well. After 16 hr, cells were subject to conditions of the indicated experiments. Cells were incubated for 24 hr in their experimental conditions and cell viability was measured using the CellTiter-Blue viability assay (Promega) following the manufacturer's instructions. Relative cell viability in the presence of starvation and/or compounds was normalized to the vehicle-treated controls after background subtraction.

Lipid peroxidation measurement

Cells were plated in 6-well dishes and followed by indicated treatments. After treatment, cells were incubated with fresh medium containing 2 μM BODIPY 581/591 C11 dye (Invitrogen: D3861) for 15 min. Cells were next collected and washed twice with ice-cold PBS followed by fluorescence-activated cell sorting (FACS) analysis using Thermo Fisher Attune NxT. Fluorescence captured during analysis was gated and plotted using FCS Express 7.

Chromatin immunoprecipitation

Cells were cross-linked using 1% formaldehyde for 10 min at room temperature. The cross-linking reaction was quenched with 250 mM Glycine for 5 min. 500 μL. Cells were lysed in lysis buffer (5 mM HEPES pH 8.0, 85 mM KCl, 0.5% NP-40, protease inhibitor mix) followed by centrifugation at 1000 g for 5 minutes at 4°C. The cell pellet was resuspended in 400 μL RIPA Buffer (PBS, 1% NP-40, 0.1% SDS, 0.5%

sodium deoxycholate, protease inhibitor mix) on ice for 20 min. Cell lysates were subjected to sonication (Bioruptor) for 15 s on and 30 s off for 15 min at highest setting to achieve a mean DNA fragment size of 200-1000 bp. Lysates were then clarified by centrifugation at 21,000 g at 4 °C for 15 min and the supernatant was collected. The AhR antibody was added and the mixture was rotated overnight. Pre-cleared protein A/G beads were mixed with 100 μg BSA and 100 μg sonicated sperm DNA followed by incubation with the lysates for 2 h. Beads were washed sequentially by lysis buffer, high salt buffer (1% TrionX-100, 0.1% sodium deoxycholate, 50 mM Tris-HCl pH 8.0, 0.5 M NaCl, 5 mM EDTA), LiCl immune complex wash buffer (0.25 M LiCl, 0.5% NP-40, 0.5% sodium deoxycholate, 10 mM Tris-HCl pH 8.0, 1mM EDTA), followed by two washes with TE buffer (10 mM Tris-HCl pH 8.0, 1mM EDTA). The protein-DNA complex was eluted by adding 200 ul freshly prepared elution buffer (1% SDS, 0.1 M NaHCO3) with rotation at room temperature for 15 min. The reverse crosslinking was carried out by adding 10 ul 5M NaCl and incubated at 65°C overnight or 4 h, followed by adding 10 μL 0.5M EDTA, 20 μL Tris-HCl pH 8.0, 1 μL of proteinase K and RNase A at 50°C for 1 h. DNA was purified by phenol/chloroform and chloroform extraction and isopropanol precipitation. The primers used for downstream qPCR were listed in key resources table.

Untargeted metabolomics

Approximately 1 million cells were plated on a 10 cm cell culture dish for overnight followed by cysteamine treatment (0.1 mM) for 4 hr. Cells were washed twice in ice-cold PBS buffer followed by addition of 80% ice-cold methanol. Cells were collected using cell scrapper and vortexed at 1800 rpm for 5 min. The mixture was sonicated in Ultrasonic bath for 20 min followed by centrifugation at 14,000 g for 10 min at 4°C to pellet the cell debris. Supernatants were subjected to metabolomics analysis using a Vanquish UHPLC coupled online to a Q Exactive mass spectrometer (Thermo Fisher Scientific). Both C18 and HILIC with positive and negative modes were conducted. Data were analyzed using Compound Discoverer 3.1 (Thermo Fisher Scientific).

In vitro transcription

Plasmid containing the sequence of eGFP was used as a template for PCR reactions to generate the desired CysRx and control sequences. Transcription reactions were performed at 37°C for 2 hours using the mMESSAGE mMACHINE T7 Transcription Kit (Invitrogen 1344). Buffer conditions for the reaction contained 50mM Tris [pH 7.8], 1mM MgCl2, 5mM KCl, and 0.8mM DTT. Triphosphate-derivatives of N1-methylpseudouridine (Ψ) (APExBIO: B8049) were used in place of UTP to generate modified nucleoside-containing RNA. The synthesized RNAs were capped by adding 6 mmol/L purified Vaccina capping enzyme, 0.5mM GTP, and 0.1mM SAM to the reaction. The reaction occurred at 37°C for an additional 2 hours. Following transcription, the template plasmids were digested with Turbo DNase. RNAs were then poly(A) tailed following the manufactures instructions (Invitrogen: AM1350). Reactions were terminated using 2.5 M lithium chloride, and RNAs were ethanol precipitated overnight at −20°C. RNAs were pelleted by centrifugation, washed with 75% ethanol and then reconstituted in nuclease-free water. The concentration of RNA was determined by measuring the optical density at 260 nm.

Cell fractionation

MEF cells were grown in four 15cm dishes until 80% confluent (~3 × 10^8 cells) followed by washing twice with ice-cold PBS. Lysosomes were isolated with lysosome isolation kit (Thermo Fisher - 89839) according to the instructions with the following optiprep gradients (8%, 12%, 16%, 19%, 23%, 27%). Lysosomes were enriched in fraction #2 (12%-16%), and mitochondria were enriched in fraction #4 (23%-27%).

Colony formation on soft agar

A solid base layer was formed by coating a 6-well plate with 2 mL of 0.6% agarose in DMEM growth media. After 30 minutes at 24°C, 1000 cells/mL were mixed with 0.5mL of 0.3% low melting point agarose and 4.5mL of DMEM growth media. One milliliter of the mixture was seeded onto the 6-well plate coated with base agar. Cells were allowed to grow for 21 days. Colonies were photographed and counted. For CysRx treatment, cells were treated with either 3ug or 5ug of CysRx on day 1, which was placed directly into the top layer mixture.

Formulation of mRNA-loaded TT3 lipid nanoparticles

TT3 lipid nanoparticles were formulated as previously described.[37] Briefly, TT3, 2-dioleoyl-sn-glycero-3-phosphoethanolamine (DOPE), cholesterol, 1,2-dimyristoyl-snglycerol, methoxypolyethylene glycol (DMG-PEG2000) were mixed at a molar ratio of 20/30/40/0.75 at the ethanol phase. CysRx or Control mRNA (TT3: mRNA=10: 1, mass ratio) was diluted in citrate buffer as the aqueous phase. TT3 lipid nanoparticles were prepared by mixing 1 volume of the ethanol phase with 3 volume of the aqueous phase using a microfluidic device (Precision NanoSystems, Vancouver, BC, Canada).

Xenotransplantation of UMRC6 cells

One million UMRC6 (shScramble, shCTNS, and/or shSlc7a11) cells suspended in 100 μL 1× PBS and 100 μL Matrigel were injected subcutaneously, bilaterally on the flanks of NOD.*Cg-PrkdcscidIl2rgtm1Wjl*/SzJ (NSG) mice. Mice were monitored for tumor growth three times per week using digital calipers. Health and body condition were also monitored concurrently. Animals were sacrificed by CO_2 euthanasia (3.5L/min) when tumors reached humane endpoint of 2000mm^3 or body condition started to deteriorate. Tumors were excised from the flank using a surgical 10 blade, weighed and flash frozen or fixed in 4% PFA.

CysRx treatment of UMRC6 tumors

Previously established UMRC6 tumors were immediately excised from CO_2 euthanized mice and minced using a surgical 10 blade. Approximately 2-3mm^3 portions of tumor were bilaterally implanted into 6–8-week-old NSG mice. Animals were monitored for tumor growth and randomized into treatment groups when tumors reached 150-200mm^3 in size. IKE/vehicle treated animals received intraperitoneal injections every other day (10 mg/kg). CysRx-TT3 treatment was conducted via weekly intratumoral (IT) injections (100uL) for three weeks. Tumors for IT injections were demarcated into four quadrants and an equal volume (25uL) of CysRx-TT3 was injected into each quadrant. HiBit-TT3 was injected into the other flank as control. Mice were monitored for tumor growth three times per week using digital calipers. Health and body condition were also monitored concurrently. Animals were sacrificed by CO_2 euthanasia (3.5L/min) one week after final administration or when the body condition started to deteriorate. Tumors were excised from the flank using a surgical 10 blade, weighed and either flash frozen or fixed in 4% PFA.

Magnetic resonance imaging of mice

Magnetic resonance imaging (MRI) of mice was conducted using a 1T M3 compact MRI from Aspect Imaging Ltd. Mice were anesthetized using 2.5% isoflurane and placed onto the specimen arm, coil was then placed around the subject and fixed in place. Mice were scanned using a T2 weighted scan without contrast agent, slice thickness was set to 1mm, with an inter-slice gap of 0mm, A total of 20 slices were obtained per animal. Raw image DICOMS were exported from MR system and imported into VivoQuant image analysis software by Invicro, a Konica Minolta Company. A tumor region of interest layer was created using automatic thresholding settings and a thickness of 5; the tumor was followed and highlighted throughout the image stack. Minor, manual modifications were made to the automatic tracing of the tumor when extraneous anatomy was included in the tumor region of interest. Once the tracing was complete a 3-dimensinal render was created and outputted into an animated GIF format.

Immunohistochemistry

Tumors were excised from mice and flash frozen in liquid nitrogen, followed by embedding in O.C.T. (Tissue-Teck: 4583). Tissue sections (15 μm thickness) were created using a Leica Cryostat (CM1950). Slides were dehydrated for 20mins at room temperature, followed by fixing using 4% PFA for 7 mins. Slides were then rehydrated in graded alcohols and stained with hematoxylin and eosin (H&E) or by immunohistochemistry. For immunohistochemistry, antigen retrieval was completed by microwaving slides at high power in citrate buffer [pH 6.0] for 21 mins. Slides were immersed in 25% hydrogen peroxide in methanol for 10 mins to inhibit endogenous peroxidase activity. Slides were blocked in BSA to prevent non-specific antibody binding for 45 mins, and then incubated with 4HNE (Abcam: ab46545) antibody overnight at 4°C. The next day, slides were incubated in biotinylated secondary antibody, followed by streptavidin HPR conjugate (Invitrogen Histostain) at room temperature. Immunoreactivity was visualized using DAB (Invitrogen), counterstained with hematoxylin (Fisher CS401-1D), dehydrated and mounted. Slides were scanned using a Leica DMi8 microscope and analyzed using Image J. A minimum of five focal planes (20X) per tumor were analyzed and averaged to quantify 4HNE positive cells.

QUANTIFICATION AND STATISTICAL ANALYSIS

Data are presented as mean ± SEM, unless otherwise stated. At least three independent biological replicates have been performed for each experiment. The number of independent experiments is indicated. Statistical tests used and specific p values are indicated in the figure legends.

RNA-seq analysis

To align sequencing reads, the 5′ and 3′ adapters of the reads were trimmed by Cutadapt (version 2.8) using the following parameters: -g "∧GGG" -a "A{10}" -n 2 -m 15 –max-n=0.1. The trimmed reads with length shorter than 15 nucleotides were excluded from the analysis. To keep accurate reading frame, low-quality bases at both ends of the reads were not subject to clip. The trimmed reads were first aligned to rRNAs using Bowtie (version 1.2.3) with the following parameters: -v 0 –norc. rRNA sequences were downloaded from the nucleotide database of NCBI and RNAcentral.[51] The reads unaligned to rRNAs were then mapped to the custom mouse transcriptome using STAR (version 2.7.10a) with default parameters. To avoid ambiguity, reads mapped to multiple positions or with >2 mismatches were disregarded for further analysis. Differential expression of genes was analyzed using edgeR separately for each pair of conditions. Calculated p values were adjusted for multiple comparison with the Benjamini-Hochberg method. Genes with fold change >2 and adjusted p value >0.05 were defined as differentially expressed genes.